This is an *Accepted Manuscript*, which has been through the Royal Society of Chemistry peer review process and has been accepted for publication.

Accepted Manuscripts are published online shortly after acceptance, before technical editing, formatting and proof reading. Using this free service, authors can make their results available to the community, in citable form, before we publish the edited article. We will replace this *Accepted Manuscript* with the edited and formatted *Advance Article* as soon as it is available.

You can find more information about *Accepted Manuscripts* in the **Information for Authors**.

CrystEngComm

HIGHLIGHT

Tuning of the crystal engineering and photoelectrochemical properties of crystalline tungsten oxide for optoelectronic device applications

Jin You Zheng, Zeeshan Haider, Thanh Khue Van, Amol Uttam Pawar, Myung Jong Kang, Chang Woo Kim and Young Soo Kang*

The photocatalysis, chromism, and sensing capabilities of nanostructured tungsten oxides, such as tungsten trioxide (WO_3), its suboxides (WO_x, 0<x<3) and hydrates ($WO_3 \cdot nH_2O$, n = 1/3 (0.33), 0.5, 0.75, 1, 2, etc.); the tungsten bronzes M_xWO_3 (M = Li, Na, K, Rb, Cs and NH_4); and metal tungstates (such as Bi_2WO_6 and $CuWO_4$) have attracted much attention. To improve these properties, many strategies have been pursued, such as morphology control, doping, and heterostructuring. Crystal facet engineering has recently become a very important method of fine-tuning the physicochemical properties of semiconductors. The photocatalytic reactivity of a photocatalyst is significantly affected by its surface environment, including its surface electronic and atomic structures, which strongly depend on the crystal facets. It is believed that crystals with different exposed facets will have different properties, with the exposure of highly activated facets enhancing the photocatalytic and sensing properties. This article describes the synthesis of 2D WO_3 crystals with the {002} facet primarily exposed, octahedral WO_3 or $WO_3 \cdot nH_2O$ with exposed {111} facets, and WO_3 films with dominant orientations, such as orientation along the {002} facet. WO_3 doping, WO_3-based heterostructuring and their applications are also presented in this paper.

1. Introduction

Environmental contamination and the continual depletion of fossil fuel reserves are urgent problems due to the rapid growth of the global population. The development of green and renewable technologies for environmental remediation and energy production is critical to solving these problems.[1] Solar energy based on semiconductor photocatalysts has attracted worldwide attention for the photodegradation of organic pollutants, water splitting, and CO_2 reduction. TiO_2, ZnO, α-Fe_2O_3, $BiVO_4$, and WO_3 are the most popular semiconductor photocatalysts. Among them, WO_3 is a typical n-type $5d^0$ transition metal oxide semiconductor with an indirect band gap (E_{BG}) of ~2.8 eV, which allows for the absorption of solar light in the visible range. The use of WO_3, the original low-band-gap metal oxide alternative to TiO_2 for the photoelectrolysis of water,[2] was first reported shortly after the initial water photoelectrolysis demonstration using TiO_2.[3] Its E_{bg} is less than those of TiO_2 (~3.2 eV) and ZnO (~3.2 eV) and greater than those of α-Fe_2O_3 (~2.2 eV) and $BiVO_4$ (~2.4 eV). Because its E_{bg} is rather large, the absorption band of WO_3 is narrow (λ < 450 nm when E_{bg} ~2.8 eV), even in the visible range. WO_3 has many interesting inherent properties, such as good hole mobility (10 cm^2 $V^{-1}s^{-1}$) and long diffusion length (150 nm), which are superior to those of α-Fe_2O_3 (10^{-2}–10^{-1} cm^2 V^{-1} s^{-1} and 2–20 nm, respectively).[4] In addition, WO_3 has good photosensitivity, good electron transport properties, and

stability against photocorrosion.[5] It also has a valence band edge with a sufficiently positive potential to oxidize water (E_{VB} ~ 3.1 V vs NHE at pH = 0); however, unfortunately, the potential at the bottom of the conduction band edge (E_{CB} ~ 0.3 V vs NHE) is below the hydrogen redox ($E_{H2}/_{H2O}$ = 0 V vs NHE) and CO_2 reduction potentials ($E_{CO2/CH4}$ = 0.169 V, $E_{CO2/CH3OH}$ = 0.016 V, $E_{CO2/HCOOH}$ = -0.25 V and $E_{CO2/CO}$ = -0.106 V; all vs NHE at pH = 0).[6] Therefore, WO_3 nanoparticles can be used as a photocatalyst for water oxidation to evolve O_2 in the presence of electron sacrificial agents (sacrificial oxidants, such as Ag^+, Ce^{4+} and $S_2O_8^{2-}$) or redox mediators (such as I^-/IO_3^- and Fe^{3+}/Fe^{2+}) to provide the driving force for the reaction.[7] A WO_3 photoanode in a photoelectrochemical (PEC) cell can only drive half of the water-splitting reaction for O_2 evolution under an applied external bias or with the assistance of another special p-type photocathode, such as p-$GaInP_2$,[8] p-Cu_2O,[9] or p-Si.[10] As described well in a recent review by Huang *et al.*,[11] an ideal photocatalyst/photoanode for water oxidation should exhibit several critical criteria, such as (1) thermodynamically favourable VB levels that are more positive than 1.2 V vs RHE (reversible hydrogen electrode); (2) high light absorption efficiency over a broad light absorption band to make full use of the solar energy; (3) effective transfer and separation of photo-induced charge carriers (electrons and holes: e^- and h^+) to suppress charge recombination; (4) sufficient surface area to provide enough active sites; (5) quick surface reaction kinetics for O_2 evolution; (6) high chemical

stability in aqueous media; and (7) low fabrication cost. With a band gap energy of 2.6–2.8 eV, WO_3 can convert approximately 6% of standard sunlight into hydrogen.[12] Its theoretical maximum solar-to-hydrogen (STH) efficiency is 4.8%, with a maximum photocurrent density of 3.9 mA cm^{-2} under AM 1.5 G irradiation (100 mW cm^{-2}), as shown in **Fig. 1**.[13] Augustynski and co-workers[14] have optimized the solution-based preparation of nanostructured WO_3 thin film electrodes to achieve an incident photon-to-electric current efficiency (IPCE) of up to 90% and photocurrents in the range of 2–3 mA cm^{-2} with an external bias (customarily reported at the water oxidation potential, 1.23 V vs RHE). Recently, Sivula and his co-workers presented a device based on a WO_3 photoanode and a dye-sensitized solar cell (WO_3/DSC) with an STH efficiency of 3.1%.[15]
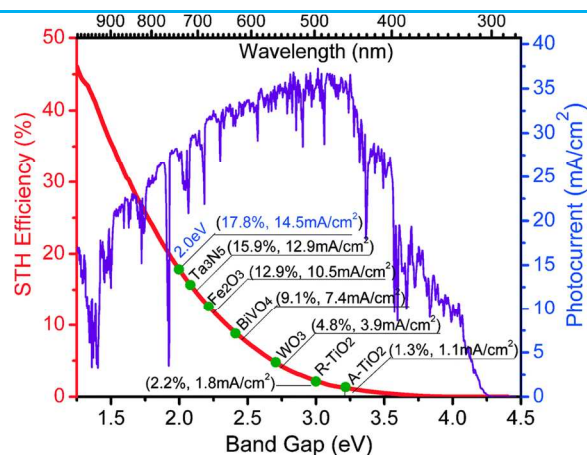

Fig. 1 Dependence of the theoretical maximum solar-to-hydrogen (STH) efficiency and the photocurrent density of photoelectrodes on the band gap under AM 1.5 G irradiation (100 mW cm^{-2}). Reproduced from Ref. 13 with permission from the Royal Society of Chemistry.

To improve the photocatalytic properties of photocatalysts, many strategies have been pursued, such as morphology control, use of macro/meso-porous structures, crystal facet engineering, metal and non-metal doping, and heterostructuring. Several review articles discuss nanostructure-based WO_3 photoanodes for photoelectrochemical water-splitting[16], state-of-the-art theoretical research activities based mainly on density functional theory (DFT) calculations for the development of efficient photoanode materials including WO_3,[17] and the synthesis of WO_3 with different dimensionalities.[18] This article highlights the synthesis of 2D WO_3 crystals with the {002} facet primarily exposed, octahedral WO_3 or $WO_3 \cdot nH_2O$ with exposed {111} facets, and WO_3 films with dominant orientations such as along the {002} facet. WO_3 doping, WO_3-based heterostructuring and their applications are also presented in this paper.

2. Crystal structures of tungsten oxides and their derivatives

WO_3 crystals have an ABO_3 perovskite-like structure and are generally constructed by sharing the corners and edges of WO_6 octahedra.[19] Pure WO_3 crystals show at least five phase transitions from −180 to 900 °C: tetragonal (α-WO_3, > 740 °C) → orthorhombic (β-WO_3, 330–740 °C) → monoclinic I (γ-WO_3, 17–330 °C) → triclinic (δ-WO_3, −43–17 °C) → monoclinic II (ϵ-WO_3, < −43 °C).[16a,19-21] Among the five crystal

forms, γ-WO_3 is the most stable phase in bulk WO_3 at room temperature. Thus, "WO_3" generally refers to γ-WO_3. A hexagonal (h-WO_3) crystal structure is also relatively stable, but it will transform into γ-WO_3 when annealed at temperatures above 400 °C.[22] The phase transition temperature of nanostructured-based WO_3 is generally lower than that of bulk WO_3.[16a] The orthorhombic crystal phase can be retained in some nanostructured WO_3 at room temperature.[23] In addition, α-WO_3, which is stable only above 725 °C, can also be retained using a low cooling rate.[24]

Because the WO_3 lattice can withstand a considerably large oxygen deficiency,[19] many tungsten suboxides (WO_x, 0 < x < 3) can exist, such as $W_{20}O_{58}$ ($WO_{2.9}$),[25] W_5O_{14} ($WO_{2.8}$),[26] $W_{18}O_{49}$ ($WO_{2.72}$),[27] W_3O_8,[28] W_2O_5,[29] WO_2,[30] WO,[30b] and W_3O.[30b,31]. The numerous forms of stoichiometric WO_3 also make it difficult to characterize comprehensively.[18a] WO_3 hydrates ($WO_3 \cdot nH_2O$, n = 1/3 (0.33), 0.5, 0.75, 1, 2, etc.), a subfield of tungsten oxides, are important because of their close relationship to WO_3 and WO_x.[19] Many crystalline hydrated tungsten trioxide compounds with the general formula $WO_3 \cdot nH_2O$ with n = 1/3 (0.33), 0.5, 0.75, 1, 2, etc., have been reported.[32] Their crystal phases are orthorhombic $WO_3 \cdot 0.33H_2O$,[33] cubic $WO_3 \cdot 0.5H_2O$,[34] orthorhombic $WO_3 \cdot H_2O$[35] and monoclinic $WO_3 \cdot 2H_2O$.[36] $WO_3 \cdot H_2O$ can be obtained through the removal of inter-layer water from $WO_3 \cdot 2H_2O$.[37] All WO_3 hydrates can be dehydrated and finally transformed into WO_3 by calcination at high temperature.

Tungsten bronzes M_xWO_3 (M = Li, Na, K, Rb, Cs and NH_4) have attracted much attention due to their wide variety of crystal structures and many interesting properties, such as their electrochromic, optical-electrical, and superconductive properties.[38] Among them, $(NH_4)_xWO_3$ can be transformed to h-WO_3 or m-WO_3 at different temperatures,[38i,39] making it an intermediate for the fabrication of WO_3 nanostructures. In addition, many metal tungstates, such as $CaWO_4$,[40] $FeWO_4$,[41] $CoWO_4$,[42] $NiWO_4$,[43] $CuWO_4$,[6b,44] $ZnWO_4$,[45] Bi_2WO_6,[46] $PbWO_4$,[47] and $CdWO_4$,[48] have been studied for different applications. For example, $CuWO_4$ has been studied for PEC water splitting[6b,44] and Bi_2WO_6 for CO_2 reduction.[46a-c,f,49]

3. WO_3 crystal facet engineering

Nanostructured tungsten oxides have been synthesized by various approaches, including both vapour- and liquid-phase-based methods.[19] Vapour-phase deposition approaches include direct current (DC) or RF sputtering, thermal evaporation deposition, e-beam deposition, pulsed-laser deposition (PLD), and arc-discharge deposition.[19] Liquid-phase-based synthesis methods include the sol-gel process[19] dip-coating, spin-coating, drop-casting, inkjet printing,[50] templating,[19] the hydrothermal method,[19] electrochemical anodization,[16a,c,d] and electrodeposition.[16a,d] The photocatalytic reactivity of a photocatalyst is significantly affected by its surface environment, such as its surface electronic and atomic structures, which critically depend on the different crystal facets.[21,51] The tuning of the surface atomic structure by crystal facet engineering can easily adjust the properties of the semiconductor, such as the electronic band structure, surface energy and surface active sites, the adsorption of a reactant, and the desorption of reaction products.[52] The crystal facet engineering of semiconductors such as TiO_2[53] and $BiVO_4$[11,54] has become a very important means of fine-tuning their physicochemical properties. To obtain nanostructures with specific exposed facets and hierarchical structures, tungsten oxides can be synthesized with 0D (quantum dots and nanoparticles with specific exposed facets), 1D (rods, wires/fibres, needles/tips, tubes, hemi-tubes and belts), 2D (nanoplates, nanoleaves, and quantum sheets)

and 0/1/2D-based hierarchical 3D structures (flower-like, brush-like, forests, hierarchical arrays, and 3D networks).[18] Because the different facets endow the material with different properties, fine-tuned WO_3 nanoparticles with specific facets are very important. Recent review articles have provided details on WO_x nanostructures and their synthesis methods.[18,19] Several review articles have focused on WO_3-based nanostructured photoelectrodes for photoelectrochemical water splitting.[16a,c,d] In this section, we will focus on the fine-tuning of WO_3 nanoparticles by exposing specific facets and WO_3-based films with dominant facets, such as nanoplates and polyhedrons.

3.1 . WO_3 crystals with {002} facets

The photocatalytic reactivity of a semiconductor photocatalyst is critically affected by its electronic and surface atomic structures, which depend strongly on the presence of crystal facets with different orientations.[51] Guo *et al.*[55] reported that the preferential orientation of the (002) planes in nanoporous WO_3 provides better conditions for the adsorption and redox reaction of pollutants than the preferential orientation of the (020) planes. Valdés *et al.*[56] found using density functional theory (DFT) calculations that the photo-oxidation of water on γ-WO_3 surfaces requires an overpotential of 1.04 V for (200), 1.10 V for (020), and 1.05 V for (002). Most recently, Xie *et al.*[57] reported that a quasi-cubic-like WO_3 crystal (with {002}, {200}, and {020} facets) with a deeper valence band maximum shows a much higher O_2 evolution rate in photocatalytic water oxidation than a rectangular sheet-like WO_3 crystal ({002}-dominant). The latter, with an elevated conduction band minimum of 0.3 eV, is able to photoreduce CO_2 to generate CH_4 in the presence of H_2O vapour, as shown in **Fig. 2**. The
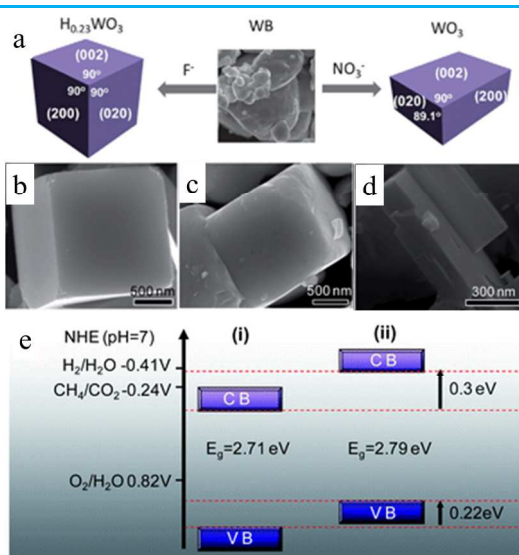
surface energy order is {002} (1.56 J m^{-2}) > {020} (1.54 J m^{-2}) > {200} (1.43 J m^{-2}), which indicates that {200} is the most stable and {002} the least stable.[57] Our group obtained a similar surface energy order using theoretical calculation, and we believe that the most reactive low-index surface in γ-WO_3 is the {002} plane.[21] Chen *et al.*[58] reported that an ultrathin single-crystal monoclinic-phase WO_3 nanosheet (**Fig. 4b,c**) of ~4–5 nm thickness was synthesized with a laterally oriented attachment of tiny WO_3 nanocrystals formed using a solid–liquid phase arc discharge route in an aqueous solution. Size-quantization effects in this ultrathin nanostructure allow the WO_3 band gap to be altered to improve its photocatalytic reduction of CO_2 in the presence of water to CH_4 relative to the performance obtained using the bulk form. Han *et al.*[59] reported the successful synthesis of triclinic sheet-like WO_3 particles with exposed (001), (100) and (010) facets by the gradual hydrolysis of $Na_2WO_4 \cdot 2H_2O$ to form WO_3 in the presence of hydrochloric acid solution (37.5%) and tartaric acid, as shown in **Fig. 3**. The average thicknesses of the WO_3 nanosheets can be tuned from 30–35 nm to 155–175 nm by changing the amount of tartaric acid used. Monodisperse WO_3 nanoparticles with more (010) facets exposed exhibit better gas sensing properties toward 1-butylamine.
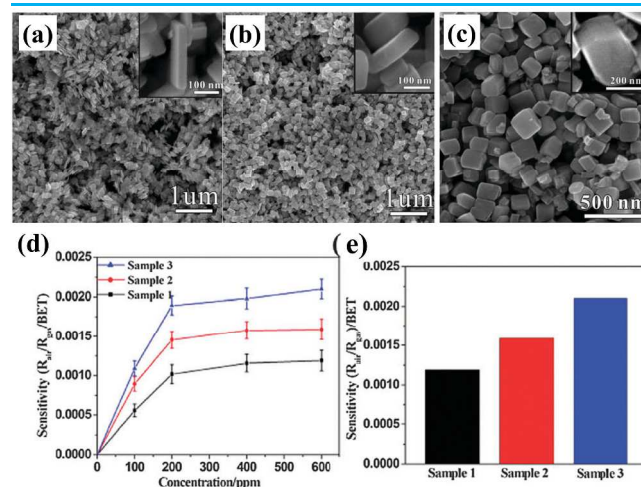

Fig. 3 SEM images of triclinic-phase WO_3 nanoparticles prepared in the presence of different amounts of tartaric acid: (a) 0.11 mol L^{-1} (sample 1), (b) 0.22 mol L^{-1} (sample 2) and (c) 0.31 mol L^{-1} (sample 3). (d) Sensitivity curves for WO_3 particles as a function of the concentration of 1-butylamine, R = resistance. (e) Sensor response to 600 ppm 1-butylamine of WO_3 particles. Reproduced from Ref. 59 with permission from the Centre National de la Recherche Scientifique (CNRS) and the Royal Society of Chemistry.

Fig. 2 (a) Schematics of the growth of a cubic $H_{0.23}WO_3$ crystal and a rectangular sheet-like monoclinic WO_3 crystal from a WB precursor in HF and HNO_3 aqueous solutions; (b) SEM image of cubic $H_{0.23}WO_3$ crystals; (c) SEM image of quasi-cubic-like WO_3 crystals obtained by calcining the cubic $H_{0.23}WO_3$ crystals; (d) SEM image of rectangular sheet-like WO_3 crystals. (e) The determined valence band and conduction band edges of two types of WO_3 crystals vs NHE (pH = 7), where quasi-cubic-like crystals and rectangular sheet-like crystals are denoted as (i) and (ii), respectively. Reproduced from Ref. 57 with permission from the Royal Society of Chemistry.

Zheng and co-workers[60] reported that monoclinic WO_3 nanoplates (**Fig. 4a**) can be successfully synthesized by a one-step template-free hydrothermal method using a topochemical conversion process of H_2WO_4 nanoplates. The γ-WO_3 nanoplates are approximately 100–170 nm in side length and 30–50 nm in thickness and exhibit superior photocatalytic activity for the degradation of rhodamine B (RhB) under visible light irradiation, which may be attributed to their high crystallinity and high BET surface area. After calcination at 600 °C for 2 h, the WO_3 catalyst shows a much enhanced activity, 4.7 times higher than that of commercial WO_3 powder. They also prepared triclinic-phase WO_3 nanoplates through the topochemical transformation of the corresponding H_2WO_4 precursors synthesized by a solution-phase method.[61] In the

reaction process, the fluoroboric acid was found to not only provide an acid source but also act as a structure-directing agent. WO_3 nanoplates could be obtained by the hydrothermal treatment of H_2WO_4 nanoplates above 160 °C or calcination at higher temperatures in air. The plate-like triclinic WO_3 has an improved gas-sensing performance for ethanol with respect to sensitivity and response time due to the
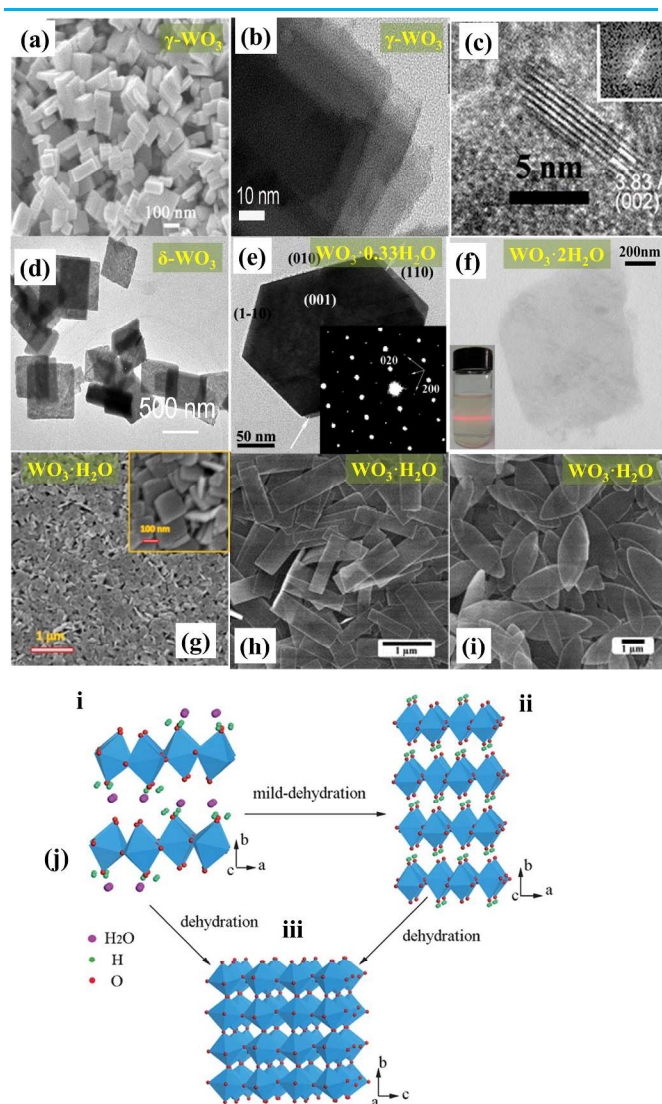

Fig. 4 SEM images of (a) γ-WO_3 nanoplates,[60] (g) $WO_3 \cdot H_2O$ nanoplates[64] and (h, i) $WO_3 \cdot H_2O$ leaf-shaped nanoplatelets (LNPs) and nanoribbons (NRs).[65] TEM images of (b, c) γ-WO_3 nanosheets,[58] (d) triclinic WO_3 (δ-WO_3) nanoplates,[61] (e) $WO_3 \cdot 0.33H_2O$ hexagonal-shaped nanodiscs,[62] and (f) $WO_3 \cdot 2H_2O$ ultrathin nanosheet.[63] (j) Schematic illustrations of the crystal structures of (i) monoclinic $WO_3 \cdot 2H_2O$, (ii) orthorhombic $WO_3 \cdot H_2O$, and (iii) monoclinic γ-WO_3.[66] Reprinted with permission from ref. 58 (Copyright 2012), ref. 61 (Copyright 2011), ref. 62 (Copyright 2008) American Chemical Society; Ref. 60 (Copyright 2014), ref. 64 (Copyright 2013), ref. 65 (Copyright 2014) Elsevier; ref. 63. Copyright 2013, Nature Publishing Group. Reproduced from Ref. 66 with permission from the Royal Society of Chemistry.

effective adsorption and rapid diffusion of the alcohol molecules.[61] Zhou et al.[62] synthesized orthorhombic-phase $WO_3 \cdot 0.33H_2O$ hexagonal-shaped nanodiscs composed of nanosheets via the hydrothermal treatment of an aqueous

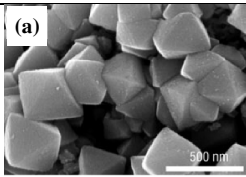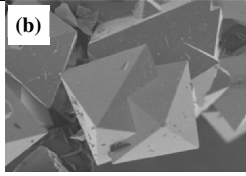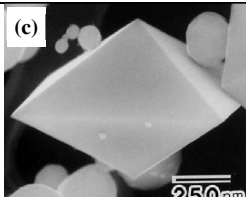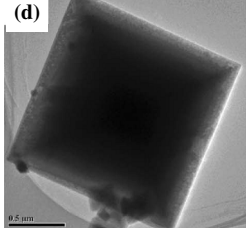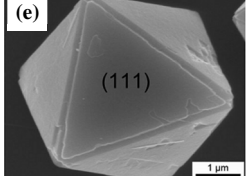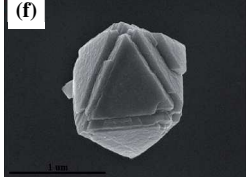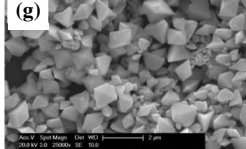peroxo-polytungstic acid solution, as shown in **Fig. 4e**, with the {001} facets mainly exposed. Xie et al.[63] reported the first synthesis of large-area nanosheets of $WO_3 \cdot 2H_2O$ (**Fig. 4f**) with a thickness of only 1.4 nm, showing much higher Li^+ diffusion coefficients than those of the bulk counterpart. $WO_3 \cdot H_2O$ nanoplates,[64] leaf-shaped nanoplatelets and nanoribbons[65] can be obtained by the hydrothermal method and the acid precipitation method. These tungsten oxide hydrate 2D structures can be transformed to 2D monoclinic WO_3 by calcination at high temperature (>300 °C). The plate-like morphology is maintained during the dehydration process, which is thought to be a topotactic process, as shown in **Fig. 4j**.[66] Finally, the {001} facet can be exposed in the calcinated samples.[61,67]

3.2 Octahedral WO_3 or $WO_3 \cdot nH_2O$

Because {111} planes are not the surfaces with the lowest surface energy, it is difficult to synthesise octahedral WO_3 crystals by a normal reaction. Few papers have reported the synthesis of octahedral WO_3 or $WO_3 \cdot nH_2O$.[24,68] These crystals can be synthesised by different methods, such as the hydrothermal, solvothermal, RF thermal plasma and solid evaporation methods.

In 2005, a report claimed the discovery of a new natural mineral species, elsmoreite, with a $WO_3 \cdot 0.5H_2O$ cubic pyrochlore structure.[32] These crystals are octahedral, and some seem to be twinned on the spinel law. In the same year, Guo et al.[24] reported that octahedral tetragonal phase WO_3 (α-WO_3) (**Table 1c**) particles were successfully produced by direct current (dc) arc discharge in Ar-O_2 gas. The octahedral crystals are bounded by 8 × {101} facets and occasionally truncated by {100} and/or {001} faces. Particle sizes of 10 nm to 1 μm with octahedral, truncated octahedral and spherical shapes were produced, depending on the production conditions, such as the gas pressure, collection position, discharge current, and cooling rate. Zhao et al.[68a] developed a new synthetic process for the production of single-crystalline γ-WO_3 octahedra (**Table 1a**) bound with {111} facets from irregular-shaped commercial WO_3 particles by a solvothermal method. Their method was based on the chemical etching of commercial WO_3 particles by corrosive NH_3 released from the decomposition of urea (WO_3 + $NH_3 \rightarrow (NH_4)_2WO_4$), the suppression of corrosion by HCl (($NH_4)_2WO_4$ + HCl → $H_2W_{1.5}O_{5.5} \cdot H_2O$ + NH_4Cl + H_2O) and subsequent recrystallization of the surface ($H_2W_{1.5}O_{5.5} \cdot H_2O \rightarrow$ H_2O + WO_3) in the solvothermal reaction. The WO_3 octahedra are covered with a thin tungstic acid shell ($H_2W_{1.5}O_{5.5} \cdot H_2O$) that stabilizes the octahedral morphology, as the {111} planes are not the surfaces with the lowest surface energy. The synthesized octahedra were nearly perfect, with a highly symmetric, regular shape containing 8 facets, 6 vertices, and 12 edges. The crystallographic stacking of (111) planes can be approximated as an alternative stacking of W- or O- on the surface, which leaves only dangling bonds of W- or O- on the surface. Therefore, the H^+ in the solution may terminate the bond and form tungstic acid on the WO_3 surface. After calcination, many cracks are formed on the surface of the octahedra, which further indicates the importance of the acid layer. The octahedra exhibit highly efficient adsorption of cations (MB) and a strong visible-light-driven ability to photocatalytically reduce metal ions. The removal efficiency of Ag^+ is approximately 11 and 74 times those of commercial WO_3 particles and P25, respectively.

Table 1 Summary of typical SEM/TEM images, structures and particle sizes, typical synthesis parameters, and properties of octahedral WO$_3$ crystals. Reproduced from Ref. 68a, 68c, 68f, 68g with permission from the Royal Society of Chemistry. Reproduced with permission from Ref. 68b, copyright 2012 Elsevier. Reproduced with permission from Ref. 24, copyright 2005 Springer.

| SEM/TEM image	Crystalline phase, Particle size, Surface area	Typical synthesis parameters	Properties	Ref.
(a)	Structure: γ-WO$_3$, $P2_1/n$, 8× {111}, H$_2$W$_{1.5}$O$_{5.5}$·H$_2$O thin layer shell Size: *ca.* 200-400 nm edge lengths Surface area: before (6.7 m^{2}g^{-1}) and after (8.2 m^{2}g^{-1}) calcination Note: Surface cracks and fractures after calcination	Precursor: 0.232 g WO$_3$, 0.5 ml 37% HCl and 1.8 g urea in 40 ml absolute ethanol Procedure: Solvothermal process, 180 °C for 12 h	Photocatalytic activities: Highly efficient adsorption of cations (MB), high visible-light-driven photocatalytic reducibility of metal ions. Ag$^+$ removal efficiency of approximately 11 and 74 times those of commercial WO$_3$ particles and P25, respectively.	68a
(b)	Structure: Twin octahedra, Cubic-phase WO$_3$·0.5H$_2$O, Fd-3 m, main exposed {111} Size: 1-10 μm edge lengths Surface area: no data	Precursor: 100 ml 0.2 M Na$_2$WO$_4$·2H$_2$O and various sulfate ion based SDAs, at pH 5.25 (controlled by 0.75 M C$_2$H$_2$O$_4$·2H$_2$O). Procedure: Hydrothermal process, 180 °C for 23 h	No data	68b
(c)	Structure: Tetragonal-phase WO$_3$, 8×{101} Size: 10 nm-1μm Surface area: no data Note: Tetragonal phase is usually only stable above 725 °C.	Precursor: W rods. Procedure: DC arc discharge in Ar-O$_2$ gases (partial pressure 33 and 13 kPa, or 65 and 25 kPa), arc current (40-100 A), low cooling rate.	No data	24
(d)	Structure: Coexistence of stable γ-WO$_3$ and metastable ε-WO$_3$, $P2_1/n$, 8×{111} Size: *ca.* 100-400 nm edge lengths Surface area: 4.88 m^{2}g^{-1} Note: ε-WO$_3$ can be converted to γ-WO$_3$ after calcination	Precursor: ammonium para-tungstate tetrahydrate powder Procedure: RF thermal plasma, air carrier gas, 30 kW, 4 M Hz.	Gas sensing properties: Octahedral WO$_3$ shows good sensing properties (response and recovery) for benzene at 400 °C with a detection limit of ~0.15 ppm, which might be due to its highly exposed {111} planes and regular octahedral shape.	68c, 68d
(e)	Structure: Cubic-phase WO$_3$·0.5H$_2$O, Fd-3m, 8×{111} Size: ca. 1-5 μm edge lengths Surface area: 8.614 m^{2}g^{-1}	Precursor: 3 ml 0.135 g/ml peroxopolytungstic acid (PTA) solution, 12 ml H$_2$O, 3.0 g Na$_2$SO$_4$ Procedure: hydrothermal process, 200 °C, 12 h	Photocatalytic activities: The WO$_3$·0.5H$_2$O octahedra possess higher photocatalytic activity for the photodegradation of methylene blue (MB) than WO$_3$·0.33H$_2$O nanoplates and WO$_3$ nanorods. This could be due to the highly reactive {111} facets of the WO$_3$·0.5H$_2$O octahedra.	68e
(f)	Structure: Hexagonal-phase WO$_3$, P6/mmm, 8×{120} Size: ca. 1 μm edge lengths Surface area: 15.26 m^{2}g^{-1} Note:	Precursor: 1.0312 g Na$_2$WO$_4$·2H$_2$O, 0.3712 g NaCl, 26 ml water, 4 ml 2 M HCl Procedure: hydrothermal process, 180 °C, 24 h	Photocatalytic activities: The exposed {120} facets of the WO$_3$ octahedra exhibited superior photocatalytic performance for the degradation of MB under visible light irradiation: 5.33 times higher than that of bulk WO$_3$ (surface area: 15.26 m^{2}g^{-1}).	68f
(g)	Structure: γ-WO$_3$, $P2_1/n$, 8× {111} Size: ca. 1 μm edge lengths Surface area: no data	Precursor: 2 g ammonium paratungstate tetrahydrate (APT·4H$_2$O), Ar gas flow rate of 2 L min^{-1} Procedure: Solid evaporation process, 1400 °C	Electrochromic properties: The octahedral WO$_3$ particle (WO$_3$-O) EC film shows a lower light transmittance modulation and charge-insertion density (H$^+$ diffusion coefficient) than the quasi-spherical WO$_3$ (WO$_3$-S) EC film.	68 g

CrystEngComm Accepted Manuscript
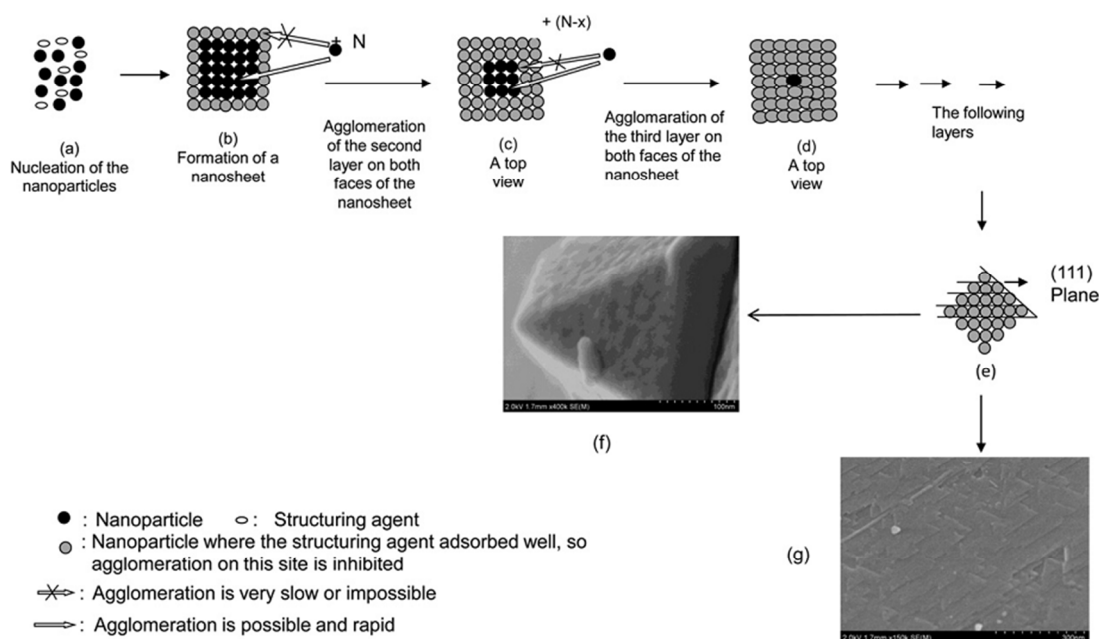
Fig. 5 Schematic illustration of the proposed growth mechanism of the WO_3 twin octahedra. HR-SEM images show cross-sectional (Fig. 5f), and planar (Fig. 5g) views of the octahedral morphology of WO_3 supporting the proposed growth mechanism. Reproduced with permission from Ref. 68b. Copyright 2012 Elsevier.

Sonia *et al.*[68b] obtained twin octahedral structures of cubic-phase $WO_3 \cdot 0.5H_2O$ (Table 1b) using sulfate-salt-based structure directing agents (SDAs) at pH = 5.25 through a hydrothermal process and explained the probable growth mechanism of the WO_3 octahedra as shown in **Fig. 5**. These SDAs include $FeSO_4$, $Fe(NH_4)_2(SO_4)_2$, $CoSO_4$, $CuSO_4$, and $MgSO_4$. The crystalline structure and morphology are influenced by the pH and both the anion and the cation of the SDA. The selective interaction of the SDA and the anion of the acidifier on the specific facets of the initially formed nanoparticles is crucial to the anisotropic growth of the nanostructures. The dielectric constant of water will decrease greatly during the hydrothermal process. The formation of WO_3 nanoparticles is enhanced because the nanoparticles formed are stabilized by adsorption by the whole SDA molecule through its cations at the negative surface sites and its anions at the positive surface sites. These WO_3 nanoparticles aggregate to form a nanosheet **(Fig. 5b)**. The SDA and the anion of the acidifier are mostly adsorbed on the periphery of the nanosheet to suppress the growth at these sites by lowering their surface energy. The second sheet can be formed by the oriented aggregation of the nanoparticles on the accessible sites on both sides of the first nanosheet **(Fig. 5c)**. The other layers of the octahedra are formed in a similar way **(Fig. 5d)**. The formation of the twin octahedra is driven by the supersaturation effect. Under the conditions of supersaturation, there is a high nucleation rate in which a crystallization unit (an atom or group of atoms) may take a sub-minimum energy position, corresponding to the birth of a second individual of a twin relative to the original.[69] This process is favoured by several factors, such as the incorporation of impurities on the surface and thermodynamic fluctuations.

Recently, a facile inorganic and green hydrothermal route for the synthesis of octahedral $WO_3 \cdot 0.5H_2O$ (Table 1e) microcrystals was reported by Shi *et al.*, as shown in **Fig. 6**.[68e] In the reaction process, by controlling the amount of Na_2SO_4,
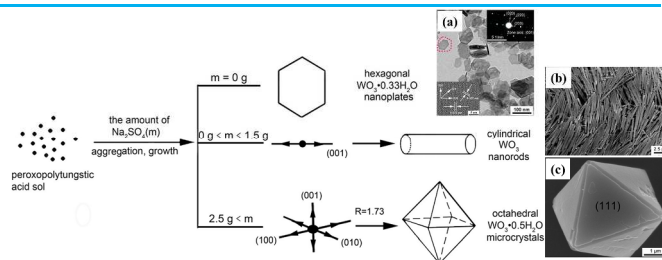
Fig. 6 Schematic illustration of the formation of $WO_3 \cdot nH_2O$ microcrystals and microscopy images of their corresponding morphologies. Reproduced from Ref. 68e with permission from the Centre National de la Recherche Scientifique (CNRS) and the Royal Society of Chemistry.

hexagonal orthorhombic-phase $WO_3 \cdot 0.33H_2O$ nanoplates (m = 0 g), cylindrical hexagonal-phase WO_3 nanorods (0 g < m < 1.5 g) and octahedral cubic-phase $WO_3 \cdot 0.5H_2O$ microcrystals (m >2.5 g) are obtained, and the morphology and crystal phase of the final products are strongly related to the Na^+ and SO_4^{2-} concentrations. The Na_2SO_4 is also an SDA because of its shape as well as its crystal phase. $WO_3 \cdot 0.5H_2O$ octahedra possess higher photocatalytic activities for the photodegradation of methylene blue (MB) than $WO_3 \cdot 0.33H_2O$ nanoplates or WO_3 nanorods. This could be due to the highly reactive {111} facets of the $WO_3 \cdot 0.5H_2O$ octahedra. Some sulfates reported in other works, such as Li_2SO_4, Rb_2SO_4, K_2SO_4, $(NH_4)_2SO_4$, $NaHSO_4$, $KHSO_4$, and NH_4HSO_4, could also direct the WO_3 crystal structure and morphology.[70] Aslam *et al.*[68f] obtained a hexagonal-phase WO_3 octahedral microcrystal (Table 1f) that is composed of eight equal facets of {120} *via* $Na_2WO_4 \cdot 2H_2O$ and NaCl assisted by a simple hydrothermal method. The exposed highly reactive {120} facets of the WO_3 octahedra exhibit superior photocatalytic performance for the degradation of MB under visible light irradiation, being 5.33 times higher than that of bulk WO_3.

Long *et al*.[68h] synthesised $WO_3 \cdot H_2O$ microcrystals with a symmetric morphology *via* a $Ni(NO_3)_2 \cdot 6H_2O$-assisted hydrothermal method. A gas-sensing investigation indicated that the annealed octahedral product possessed an enhanced sensitivity towards ethanol.

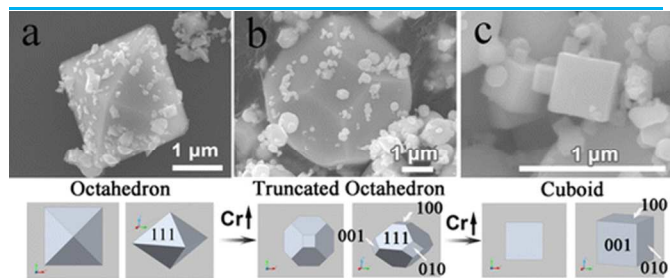**Fig. 7**. Summary of the morphology evolution and corresponding crystal growth trends (middle part is the corresponding schematic illustration): SEM images of (a) WO_3, (b) 2.5 at. % $Cr-WO_3$ and (c) 10.0 at. % $Cr-WO_3$. Reprinted with permission from ref. 68d. Copyright 2015 American Chemical Society.

Yuan's group[68c,d] successfully used the RF thermal plasma technique to prepare octahedral γ-WO_3 (Table 1d), which shows good sensing properties (response and recovery) for benzene at 400 °C, with a detection limit of ~0.15 ppm. This might be due to its highly exposed {111} planes and regular octahedral shape. The high yield production of octahedral γ-WO_3 can also be achieved by a solid evaporation method with ammonium paratungstate tetrahydrate ($APT \cdot 4H_2O$) as a precursor. Later, they also synthesized Cr-doped WO_3 polyhedra controlled by tailoring the intrinsic thermodynamic properties of the RF thermal plasma, as shown in **Fig. 7**. Together, the distortions introduced by Cr in the WO_3 matrix and the chromate layer on the crystal surface could reduce the growth rates along the [001], [010], and [100] directions. The morphology evolution occurred in the following order with increasing Cr doping: octahedron $\rightarrow$ truncated octahedron $\rightarrow$ cuboid. The highest gas sensing response was achieved by 2.5 at.% Cr-doped WO_3 polyhedra due to the co-effects of the exposed crystal facets, activation energy, catalytic effect of Cr, and particle size on the surface reaction and electron transport units.[68d] Very recently, Chang *et al*.[68g] successfully achieved the large-scale, high yield production of WO_3 nanoparticles for electrochromic applications via a high-temperature, catalyst-free, solid evaporation route with ammonium paratungstate tetrahydrate ($APT \cdot 4H_2O$) as a raw material. The particle morphologies obtained in different zones of the quartz tube include polyhedral, octahedral, and quasi-spherical. The octahedral γ-WO_3 microparticles (Table 1 g) can be synthesized at 1400 °C.

3.3 WO_3 films with dominant orientations

WO_3 films have been fabricated by many different methods, such as sputtering,[71] evaporation,[71b] chemical vapour deposition (CVD),[72] pulsed laser deposition (PLD),[73] molecular beam epitaxy,[74] sol–gel,[75] the hydrothermal method,[51] atomic layer deposition (ALD),[76] cathodic electrodeposition,[16a,d] electrochemical anodization,[16a,c,d] inkjet printing,[50b,77] and the rubbing method[21,51]. The methods for making epitaxial WO_3 films are summarized in **Table 2**.

In 1989, Kobayashi *et al*.[71a] reported that epitaxial WO_3 films were grown on MgO and various sapphire substrates via the RF magnetron sputtering method. The crystal orientation of the

films strongly depends on the substrate material and the oxygen concentration in the sputtering atmosphere. Films grown on a (100)-oriented MgO substrate had an orientation of $WO_3(001)$ along the growth direction for 60 vol% O_2. The films grown on the ($11\bar{2}0$)-oriented sapphire (α-Al_2O_3) had orientations of $WO_3(001)$ in 70% O_2 and $WO_3(021)$ in 60% O_2. The films grown on the (0001)-oriented and ($1\bar{1}02$)-oriented sapphires had orientations of $WO_3(121)$ and $WO_3(001)$, respectively. LeGore *et al*.[71b] studied the epitaxial growth of tetragonal-phase $WO_3(001)$ films on R-plane sapphire ($Al_2O_3(1\bar{1}02)$) by direct electron beam evaporation. The films obtained at room temperature were amorphous and became polycrystalline after annealing in O_2. The epitaxial films possessed better gas-sensing (H_2S) properties than the polycrystalline films. Later, Mohammad[78] used the same electron beam evaporation method to deposit (010)-oriented WO_3 on various epitaxial sapphire substrates, such as α-$Al_2O_3(\bar{1}012)$ and α-$Al_2O_3(0001)$. Tagtstrom and Jansson[72] deposited epitaxial monoclinic-phase WO_3 films with (100), (010), and (001) orientations on sapphire ($01\bar{1}2$) substrates using a hot-wall chemical vapour deposition (CVD) technique. Garg and co-workers[71c] chose $SrTiO_3(100)$ as the substrate for the DC magnetron sputtering of a WO_3 film because it has very close lattice matching (3.905 Å) with WO_3. The $WO_3(002)$ can be deposited on not only $SrTiO_3$ but also sapphire ($10\bar{1}2$). Yamamoto *et al*.[79] also reported the deposition of monoclinic $WO_3(002)$ epitaxial thin films on α-$Al_2O_3(01\bar{1}2)$ by ArF excimer pulsed laser deposition in a controlled oxygen atmosphere.
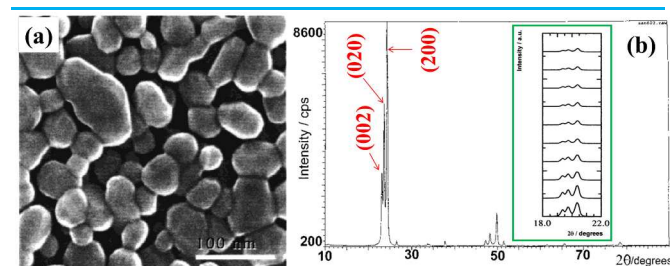
Fig. 8 Typical SEM image and XRD pattern of a WO_3 film prepared by the deposition of a tungstic acid/PEG 300 colloidal solution and annealing at 550 °C. Inset is the diffraction patterns of a WO_3 film (~1.2 μm thick) recorded at decreasing glancing angles from $\alpha = 5^o$ (bottom) to 0.5^o (top). Reprinted with permission from ref. 75. Copyright 2001 American Chemical Society.

For the formation of WO_3 nanoparticulate films, sol-gel routes based on the sintering of colloidal nanoparticles appear to be simple and viable.[16c] These methods are based on the formation of a stable H_2WO_4 sol that can be dehydrated at high temperature to form a stable WO_3 thin film. Augustynski *et al*. achieved the most promising results via this method.[75,80] They developed a route based on the preparation of an ethanolic H_2WO_4 sol by ion-exchange on a cationic resin, followed by the addition of polyethylene glycol (PEG), used as a stabilizer and dispersing agent for the subsequent blading on the TCO glass.[16c,75,80] The film annealed at 550 °C under an oxygen atmosphere has the best photoelectrochemical performance due to the formation of a transparent thin film composed of relatively large, polydisperse (*ca*. 30-100 nm) interconnected monoclinic WO_3 nanoparticles showing substantial porosity (**Fig. 8a**). The XRD patterns (**Fig. 8b**) show that the WO_3 nanocrystallites in the film are arranged in preferential orientations in the intensity order (200) > (020) > (002). The best PEC performances were obtained from 2.5 μm thick

Table 2 Summary of the epitaxial WO_3 films: method, substrate, epitaxial film orientation on substrate (confirmed by XRD) and application.

Method	Crystal structure and epitaxial relationships between the film and substrate	Notes	Applications	Ref.
RF magnetron sputtering	Monoclinic-phase WO_3 (Space group: C_{2h}^5) WO_3(001)//MgO(200) in Ar-60%O_2, WO_3(001)//Sapphire(11$\bar{2}$0) in Ar-70%O_2, WO_3(021)//Sapphire(11$\bar{2}$0) in Ar-60%O_2, WO_3(002)//Sapphire(1$\bar{1}$02) in Ar-70%O_2, WO_3(121)//Sapphire(0001) in Ar-70%O_2	The crystal orientation of the films strongly depends on the substrate materials and the oxygen concentration in the sputtering atmosphere.	No data	71a
Electron beam evaporation	Tetragonal-phase WO_3 (α-WO_3) α-WO_3(001)//Sapphire(1$\bar{1}$02)	Purely tetragonal WO_3 films could be grown only up to 30 nm thickness; an admixture of monoclinic and/or orthorhombic phases appeared in thicker films.	The epitaxial films possessed better gas-sensing (H_2S) properties than the polycrystalline films.	71b
	Monoclinic-phase WO_3 WO_3(010)//α-Al_2O_3($\bar{1}$012) WO_3(010)//α-Al_2O_3(0001)	The epitaxial growth phenomena are interpreted by nucleation and growth theories in relation to the variation of the density of the surface oxygen vacancies of the α-Al_2O_3 substrate.	No data	78
Chemical vapour deposition	Monoclinic-phase WO_3 WO_3(100)//Sapphire(01$\bar{1}$2), WO_3(010)//Sapphire(01$\bar{1}$2), WO_3(001)//Sapphire(01$\bar{1}$2)	The microstructure of the films could be controlled by the total pressure and linear gas flow velocity. The deposition process was controlled by mass transport.	No data	72
DC magnetron sputtering	Monoclinic-phase WO_3 WO_3(002)//$SrTiO_3$(100) WO_3(002)//Sapphire(10$\bar{1}$2)	$SrTiO_3$ has very close lattice matching (3.905 Å) with WO_3. The preferred orientation improved as the deposition temperature decreased.	No data	71c
Pulsed laser deposition	Monoclinic-phase WO_3 WO_3(002)//α-Al_2O_3(01$\bar{1}$2)	The crystal quality can be improved by increasing both the oxygen pressure and the substrate temperature.	Gasochromic coloration in the WO_3 films by exposure to diluted hydrogen was found to correlate with the crystal quality of the films. The gasochromic coloration was suppressed by the epitaxial growth of the films.	79
Sol-gel method (blading)	Monoclinic WO_3 WO_3(200)-(020)-(002)//FTO	The shape and size of the WO_3 nanoparticles and the porosity and properties of the films strongly depend on the preparation parameters, such as the tungstic acid/organic additive ratio and the annealing conditions.	Photoresponse to the blue region of the solar spectrum (up to 500 nm); relatively large photocurrent densities for the photooxidation of water and especially the photooxidation of various organic substances (reaching 5 mA/cm^2). Promising candidate for electrochromic device applications.	75
Cathodic electrodeposition	Monoclinic WO_3 WO_3(200)-(002)//FTO from 0.20 mol dm^{-3} tungsten WO_3(002)-(200)//FTO from 0.10 mol dm^{-3} tungsten WO_3(002)-(200)//FTO from 0.05 mol dm^{-3} tungsten	The (002) plane is favoured to an extent determined by both the tungsten concentration and deposition time. Increasing the tungsten concentration favours the (200) plane most.	Photocurrent value of 0.08 mAcm^{-2} at 0.9 V vs Ag/AgCl in 0.5 M NaCl under a 100 mW cm^{-2} tungsten-halogen lamp.	81
Doctor blading method	Monoclinic WO_3 WO_3(002)//FTO	The predominant {002}-faceted platelet-like WO_3 nanoparticles were synthesized by a microwave-assisted nonaqueous sol-gel route and prepared into photoanodes by the doctor blading method for PEC water splitting.	Photocurrent before (1.5 mAcm^{-2}) and after (2.5 mAcm^{-2}) cathodic polarization in 1.0 M H_2SO_4; 2.7 mAcm^{-2} in 3.0 M H_2SO_4 under AM 1.5 G light (1 V vs RHE, 100 mWcm^{-2})	82
Spin coating	Monoclinic WO_3 WO_3(002)-(110)//FTO	Colloidal W nanoparticles were synthesized by hot-matrix synthesis, and the metallic NPs were then spin-coated onto FTO glass substrates and transformed to the WO_3 phase by heat treatment at 500 and 550 °C.	The highest achieved photocurrent was ~830 μAcm^{-2} at 1.9 V vs RHE with a 900 nm thick film.	83
Finger-rubbing method	Orthorhombic-phase $WO_3 \cdot H_2O$ and monoclinic WO_3 $WO_3 \cdot H_2O$(020)//FTO WO_3(002)//FTO	The $WO_3 \cdot H_2O$(020)//FTO can be converted to WO_3(002)//FTO by calcination.	WO_3(002)//FTO with a film thickness of 250 nm can reach 0.38 mA cm^{-2} at 1.0 V vs Ag/AgCl under 1 sun light.	21, 51

CrystEngComm Accepted Manuscript

electrodes with saturation photocurrents exceeding 2 - 2.5 mA cm⁻² under AM 1.5 illumination.[16c] The efficient operation of the photoanodes also relies on the electron transport properties of the network of WO_3 nanoparticles. The essentially crystalline structure of the boundaries between the nanocrystals forming the preferentially orientated monoclinic WO_3 film certainly contributes to its excellent photoelectrochemical behavior.[75] Photoanodic water oxidation with photocurrents of up to 2.7 mA cm⁻² at 1.0 V vs RHE under AM 1.5 can be achieved with a 2.5 μm thick electrode in the presence of methylsulfonic acid (CH_3SO_3H) as a supporting electrolyte.[80] WO_3 films with preferred orientations can also be obtained by cathodic electrodeposition. Kwong *et al.*[81] reported that some preferred orientations can be observed in a WO_3 film on an FTO-coated glass substrate obtained by electrodeposition using aqueous solutions of peroxotungstic acid, as shown in **Fig. 9**. The (002) plane is favoured as a function of both the tungsten concentration and deposition time, while increasing the tungsten concentration favours the (200) plane most. At high concentrations (0.2 mol dm⁻³), the (200) plane is more preferred than (002), although both are preferred.
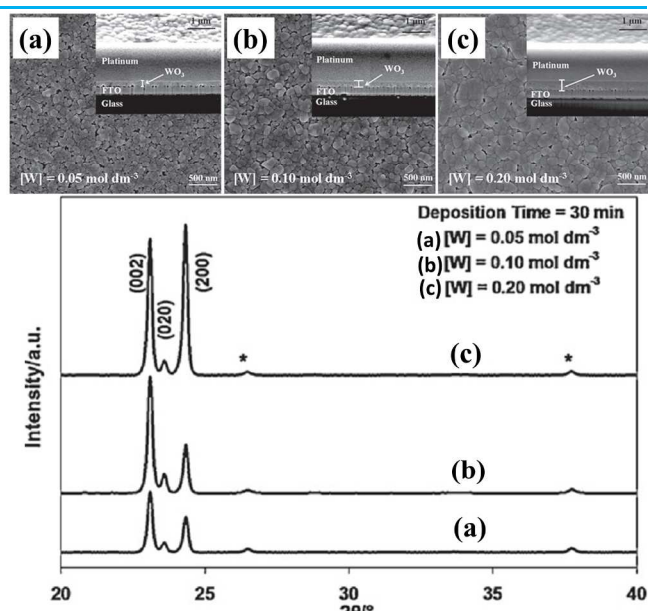

Fig. 9 SEM images and XRD patterns of WO_3 thin films electrodeposited from tungsten concentrations of (a) 0.05 mol dm⁻³, (b) 0.10 mol dm⁻³ and (c) 0.20 mol dm⁻³. Reproduced with permission from Ref. 81. Copyright 2014 Elsevier.

Hilaire *et al.*[82] reported that nanostructured WO_3 photoanodes with a crystallographic orientation along the [001] direction can be fabricated *via* doctor blading nanoparticles synthesized through a microwave-assisted nonaqueous sol-gel route, as shown in **Fig. 10**. The monoclinic WO_3 nanoparticles are platelet-shaped with a size range from 20 to 40 nm and a thickness of approximately 3 nm. The orientation of the face of the platelets is {002}. The film shows an interconnected network of nanoparticles with a clearly visible porosity and a thickness of approximately 2.3 μm. The XRD pattern shows a strong {002} out-of-plane preferred orientation, as evidenced by the enhanced intensity of the (002) and (004) reflections (**Fig. 10g**). The as-prepared WO_3 photoanode shows 1.5 mA cm⁻² at 1 V vs RHE
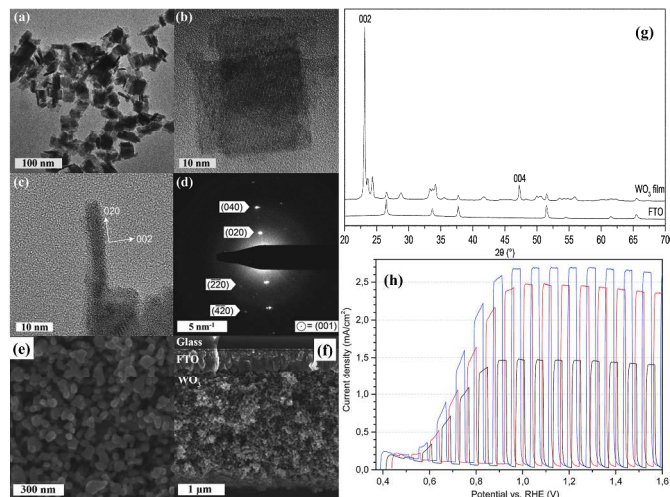

Fig. 10 TEM images of WO_3 nanoparticles synthesized through a microwave-assisted nonaqueous sol-gel route. (a) Overview of several nanoparticles; (b) platelets lying flat on the substrate; (c) platelets lying on the edge; (d) electron diffraction pattern corresponding to (b). (e) Top-view and (f) cross-section view SEM images, (g) XRD of a (002)-oriented WO_3 photoanode. (h) Photocurrent density of the WO_3 electrode in 1.0 M H_2SO_4 before (black) and after (red) cathodic polarization and in 3.0 M H_2SO_4 (blue) after polarization under AM 1.5 G chopped illumination (100 mW cm⁻²). Reproduced from Ref. 82 with permission from the Royal Society of Chemistry.

in 1.0 M H_2SO_4 (**Fig. 10h**, black curve). This photocurrent was significantly enhanced by sweeping the potential in the dark from -0.65 V to 0.1 V vs MSE prior to the measurement, and a photocurrent of 2.5 mA cm⁻² was obtained afterwards in 1.0 M H_2SO_4 (**Fig. 10h**, red curve). Upon increasing the electrolyte concentration to 3.0 M H_2SO_4, a photocurrent of 2.7 mA cm⁻² was achieved after polarization (**Fig. 10h**, blue curve). This photocurrent is comparable with the best photocurrents reported[16b] for WO_3 photoanodes to date. It is difficult to confidently attribute the good photocurrents obtained in this work to the shape or orientation of the nanoparticles because the photoelectrochemical activity can be influenced by many other factors, such as the surface area, porosity or thickness of the film.[82] Very recently, Emin and co-workers[83] reported another means of preparing textured WO_3 film from colloidal W nanoparticles. Amorphous W NPs with an average diameter of ~1.5 nm were spin-coated on FTO substrates and then transformed to the monoclinic WO_3 phase (**Fig. 11a**) by heat treatment. The as-prepared WO_3 film shows two main dominant XRD peaks corresponding to (002) and (110) (**Fig. 11b**). The highest photocurrent, which is ~830 μA cm⁻² at 1.9 V vs RHE, can be achieved with a 900 nm thick WO_3 film with back illumination (**Fig. 11c**). This value is almost three times higher than that obtained with a 200 nm thick film. In the thicker films, the collection of the photogenerated carriers is more efficient in the back configuration than in the front configuration.[83]
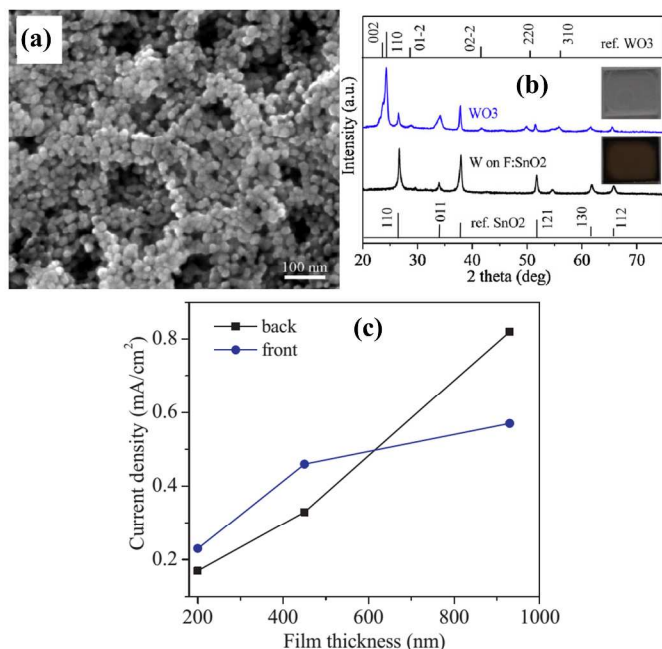
Fig. 11 (a) SEM image of WO$_3$ film obtained after the calcination of spin-coated W films at 500 °C for 60 min in air. (b) XRD spectra of W and WO$_3$ thin films on FTO substrates. (c) Relationship between photocurrent density and film thickness for WO$_3$ samples calcined at 500 °C/1 h in air. Reproduced with permission from Ref. 83. Copyright 2014 Elsevier.

Recently, our group prepared dominant (002) films by a facile finger-rubbing method.[21] The rubbing method is a useful way to rapidly and economically fabricate nano-/submicro-/microparticles with a mono-/multilayer or one-axis orientation on solid substrates, such as glass, Si wafers, TCO glasses and other substrates with smooth surfaces, without using solvents, reactors, or equipment. In addition, the rubbing method can be used to fabricate films with a one-axis orientation without needing to consider the crystal lattice matching between the rubbing materials and substrates.[21,51,84] For the rubbing process, a dilute polyethylenimine (PEI) ethanol solution was first spin-coated on the substrates. The particles were then placed on the PEI-coated substrates and rubbed smooth by a finger protected by a powder-free latex exam finger cot. The higher the rubbing force and the longer the rubbing time, the thinner the resulting film.[21] The size limitation for direct attachment by the rubbing method ranges from approximately 0.5 to 3 μm depending on the rubbing rate, closeness of packing, uniformity of the orientation of the assembled microcrystals, substrate area, and ecological considerations.[51,84a] After the rubbing process, the obtained film should be calcined to remove the PEI polymeric linker to increase the adhesion between the particles and the substrates.[84d] We have fabricated O-WO$_3$·H$_2$O nanoplates on FTO glass substrate to form (002)-oriented γ-WO$_3$ thin films with different thicknesses by finger rubbing and post-calcination; the corresponding experimental procedure is shown in **Fig. 12a**. **Fig. 12b** shows a typical SEM image of a uniform WO$_3$·H$_2$O nanoplate powder obtained by a hydrothermal method using L-lactic acid as the capping agent at 120 °C for 6 h. The average length and thickness of the nanoplates are ca. 300 nm and ca. 40 nm, respectively. The crystal structure of the as-obtained WO$_3$·H$_2$O nanoplate can be fully indexed to the orthorhombic phase WO$_3$·H$_2$O (O-WO$_3$·H$_2$O, space group: Pmnb) based on the standard card JCPDS no. 43-0679 with two main peaks corresponding to (020) and (111), as shown in **Fig. 12c(c1)**. After calcination at 500 °C for 2 h in air, the crystal structure transitions

into a pure monoclinic phase WO$_3$ (γ-WO$_3$, space group: P21/n, JCPDS no. 43-1035), with three main characteristic peaks corresponding to (002), (020), and (200), as shown in **Fig. 12c(c2)**. The as-obtained rubbing WO$_3$·H$_2$O films, except those that obtained using the FTO substrate (marked by stars), show only two main peaks corresponding to O(020) and O(040), as shown in **Fig. 12e(e1)**. This finding indicates that the (020)-oriented O-WO$_3$·H$_2$O film can be directly prepared by the rubbing method. After calcination at high temperature, the XRD patterns (**Fig. 12e(e2)**) for the post-calcinated films show only two main peaks of γ(002) and γ(004). The corresponding SEM image for the (002)-oriented γ-WO$_3$ film is shown in **Fig. 12(d).** The film is not perfect, and some nanoplates were easily broken. Three possible reasons for this are that (i) the nanoplates are approximately 300 nm in size, less than the lower size limit of 500 nm for rubbing; (ii) the thicknesses of the nanoplates are ca. 40 nm, as shown in **Fig. 12b**, and these plates can only support a limited force; and (iii) the surface of the FTO substrate is very rough at the nanoscale level.[21,51] However, the (020)-oriented O-WO$_3$·H$_2$O films can be easily converted to (002)-oriented γ-WO$_3$ films.
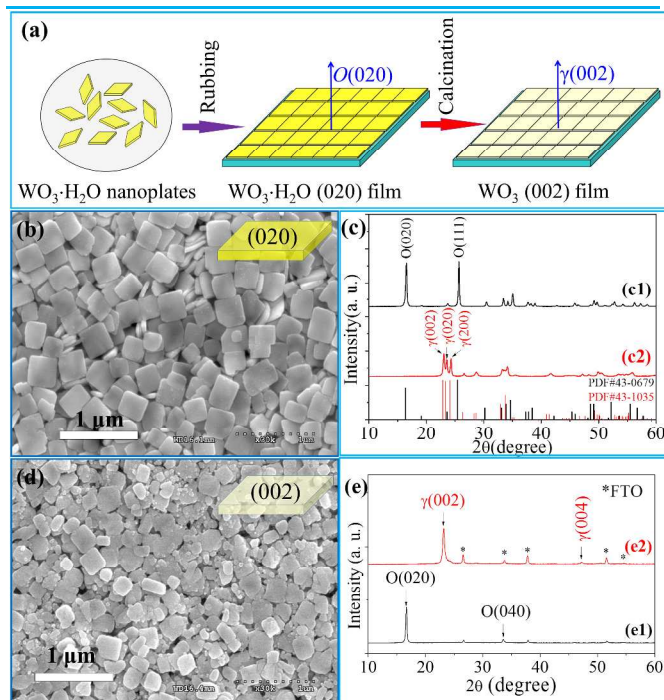
Fig. 12 (a) Schematic illustration of the fabrication procedure for a (020)-oriented O-WO$_3$·H$_2$O nanoplate thin film on an FTO glass substrate by the rubbing method and the conversion of the film to a (002)-oriented γ-WO$_3$ film by calcination in air. SEM images of (b) WO$_3$·H$_2$O nanoplate powder and (d) (002)-oriented WO$_3$/FTO film. XRD patterns of the WO$_3$·H$_2$O nanoplate powder obtained by the hydrothermal method (c1) before and (c2) after calcination. (e) XRD patterns of (e1) the O(020)-oriented WO$_3$·H$_2$O/FTO film obtained by the rubbing method and (e2) the O(002)-oriented WO$_3$/FTO film obtained by the calcination of the WO$_3$·H$_2$O/FTO film. Adapted with permission from ref. 21. Copyright 2014 American Chemical Society.

The (002)-oriented γ-WO$_3$ film prepared by the rubbing method can also be used as the seed layer for (002)-oriented nanorod growth in a hydrothermal reaction.[51] A comparison between seed layers prepared by the spin coating and rubbing methods shows that the crystallinity and dominant crystal facets of the WO$_3$ seed layers are different. The spin-coating seed

layer with a particle size of < 50 nm has low crystallinity, and the dominant crystal facet cannot be controlled artificially. In contrast, the crystallinity of the rubbing seed layer (002-oriented γ-WO$_3$ thin film) is very high, and the dominant crystal facet is γ(002). Therefore, the rubbing seed layer is effective in the formation of (002)-oriented nanorod films. In the top-view and cross-sectional SEM images of the as-synthesized WO$_3$ nanorod films prepared by the rubbing method assisted by the hydrothermal method shown in **Fig. 13a and b**, respectively, the corresponding XRD (**Fig. 13c**) pattern shows only one main (002) peak with very high intensity, with an $I_{(002)}/I_{(020)}$ of 16.73 and an $I_{(002)}/I_{(200)}$ of 25.73. This indicates that the WO$_3$ nanorods preferably grew along the [001] orientation. The current–potential property was investigated in 0.5 M Na$_2$SO$_4$ solution (pH 6.3) under chopped (1 Hz light on/off cycles) 1 sun light illumination. The photocurrent onset potential is approximately −0.1 V vs Ag/AgCl, and the photocurrent is *ca.* 0.65 mA cm^{-2} at 1.0 V vs Ag/AgCl.
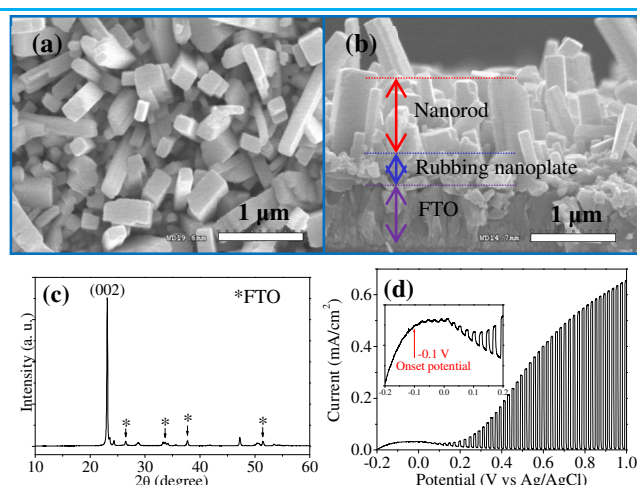

Fig. 13 (a) Top-view and (b) cross-sectional SEM images and (c) XRD pattern of the as-synthesized WO$_3$ film prepared by the rubbing method assisted by the hydrothermal method at 180 °C for 24 h using 0.1 mol citric acid as a capping agent. (d) Photocurrent of the film after calcination in air at 500 °C for 2 h. The inset is a magnified curve from -0.2 to 0.2 V. Reproduced by permission of the Royal Society of Chemistry.

4. Doping of WO$_3$ and band gap engineering

In addition to the efforts to improve the properties of the WO$_3$, such as its crystallinity, size and morphology through various strategies, studies of the doping of foreign elements into the WO$_3$ host lattice has provided significant insight into the changes of the WO$_3$ crystallographical structure and the electronic configuration, which impacts the electron transport and optical absorption behaviours as well as the activity of the material.

4.1 Transition metal element doping

There have been numerous reports on the doping of transition metals into WO$_3$ lattice structures to improve their photocatalytic activity. Transition metal dopants intercalated into the WO$_3$ structure interstitially or substitutionally with the tungsten cation cause a profound transformation of the electronic configuration of the structure and morphology, which can significantly change the physicochemical properties.

Taking advantage of this, researchers have been refining synthetic methods to retard the recombination rate of e$^-$ (electrons) and h$^+$(holes) and shift the absorption onset to the visible-light region to enhance the application performance. Water splitting for hydrogen production[85] or CO$_2$ reduction for practically usable organic compounds such as CH$_3$OH production[86] driven by the photocatalysts was significantly exploited in numerous works in the literature. Because the valence band of WO$_3$ is below the oxidation level, the oxygen evolution from the water via a WO$_3$ photocatalytic process was observed in one early report[87]

$$4h^+(WO_3) + H_2O \rightarrow O_2 + 4H^+$$
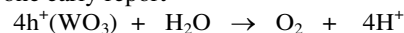
However, pure intrinsic WO$_3$ exhibits quite poor photocatalytic ability for hydrogen production. Maruthamuth et al. reported that doping Cu(II) into the WO$_3$ lattice improved the photocatalytic activity for the reduction reaction of H$^+$ to H$_2$ under
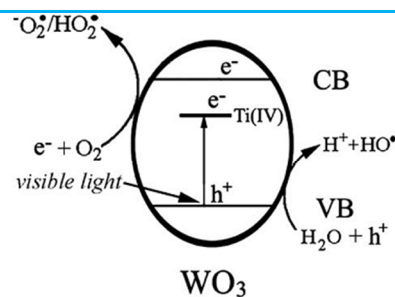
Scheme 1: Schematic diagram of the charge separation and photocatalytic activity of Ti(IV)-doped WO$_3$. Reproduced from Ref. 91 with permission from the Royal Society of Chemistry.

the assistance of MV^{2+}.[88] Studies on doping various transition metals (Fe, Co, Ni, Cu and Zn) into WO$_3$ to markedly change the photocatalytic activity have been performed by Gondal *et al*. and other groups[89]. Introducing Ti ions into the WO$_3$ lattice induces the plate band potential to shift toward positive values. The Ti-doped WO$_3$ showed profoundly superior incident photon-to-current efficiency (IPCE) relative to the undoped WO$_3$ due to the decreased photogenerated electron/hole recombination rate.[90] This result was recently confirmed by another group.[91] By using a facile, mild, aqueous-phase route, the authors have fabricated Ti(IV)-doped WO$_3$ nanocuboids that exhibit excellent visible-light-driven photocatalytic performance. Such a high photocatalytic activity enhancement is enabled by the band structure modification, as presented in **Scheme 1**. Tu and co-workers[92] prepared hierarchically structured Ti-doped WO$_3$ through a template-free hydrothermal method. The study showed the remarkable effects of the Ti dopant on the surface morphology and crystal structure, which led to improved electrochromic properties. An interesting report by Karuppasamy and co-worker showed that the introduction of 11% vanadium dopant into WO$_3$ can significantly enhance the photocatalytic efficiency of the WO$_3$ thin film.[93] The V dopant creates defects in the structure that result in an optical band gap reduction. It is stated that multivalent vanadium atoms bonding with the terminal oxygens in the WO$_3$ lattice gives rise to localized covalent bonds, resulting in an increase in the surface work function. The experimental observations reveal that V may be a good candidate for doping into WO$_3$ for applications in electrochromic materials or photocatalysis.

The photocatalytic activity of WO$_3$ was demonstrated by the degradation of NO$_2^-$ by the Leng group.[94] The photocatalytic

performance is enhanced in a Zn-doped WO_3 film grown on indium-tin oxide glass. Zn^{2+} cations alternatively incorporated with W^{6+} species in the WO_3 lattice induce efficient visible light absorption, which is beneficial for charge carrier generation. However, doping Zn into the WO_3 host material does not account for the change in the band gap energy. The properties of a WO_3 photoelectrode used for water photolysis were also investigated when tantalum ions (Ta^{5+}) were doped into the structure.[95] Ta^{5+} ions are compatible with the WO_3 structure, with similar ionic radii and chemical and optoelectronic properties. This matching is beneficial for achieving a uniform morphology and enhancing the photoconversion efficiency at a specific dopant concentration. Mo transition metal doping into the WO_3 structure can enhance the photoactivity of WO_3 nanowires.[96] The photocatalytic activity enhancement is presumed to be the result of the synergetic effects of the crystalline structure and Mo-doping. Although the work did not clarify how the photocatalytic activity of the WO_3 nanowire is increased by doping with Mo, it provides a general outlook on transition metal doping. A more detailed study by the Yu group[97] investigated the doping of alternating Mo atoms into the WO_3 structure. The work shows that W atoms can be substituted by Mo atoms up to 75% without destroying the original orthorhombic structure of $WO_3.0.33H_2O$. This is possible because the Mo atom has very similar chemical properties to W, which is in the same group (6) of the transition metals. Increasing the content of Mo atoms in the WO_3 would significantly narrow the band gap energy of $WO_3 \cdot 0.33H_2O$, which is thought to enhance the intervalency transition due to the increasing M^{5+} (M = Mo and W) fraction. In addition to the numerous works devoted to transition metal doping into WO_3 in the literature, rare earth element dopants such as cerium[98] and dysprosium[99] have also been studied. For the Dy dopant, Peng and co-workers attributed the enhancement of the WO_3 photocatalytic activity to the photocatalytic reaction mechanism for the degradation of rhodamine B, wherein the doped Dy^{3+} is oxidized by O_2 to form $\cdot O^{2-}$ and Dy^{4+} and then the Dy^{4+} is reduced back to Dy^{3+} by the photogenerated e^- from the conduction band of WO_3. The photocatalytic reactions retard the photogenerated charge carriers and accelerate the photocatalytic reaction for the degradation of rhodamine B.
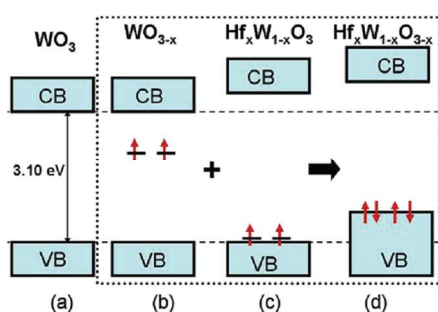

Fig. 14 Schematic representation of the band edges and impurity gap states in (a) WO_3, (b) WO_{3-x}, (c) $Hf_xW_{1-x}O_3$, and (d) $Hf_xW_{1-x}O_{3-x}$. The horizontal dashed lines represent the top of the valence band and the bottom of the conduction band of pure WO_3. Reprinted with permission from ref. 5. Copyright 2012 American Chemical Society.

Wang et al.[5,100] studied the electronic properties of doped γ-monoclinic WO_3 using DFT calculations with hybrid functionals. Doping with isovalent Mo or Cr ions narrows the band gap but shifts the CB edge downward. Replacing O with S

could narrow the energy gap by introducing localized occupied states above the VB and shift the CB minimum upward. Doping with low-valence Ti, Zr, or Hf ions widens the band gap and shifts the CB edge to higher energies. However, replacing the W with Hf induces the formation of compensating defects; in Hf-doped WO_3, oxygen vacancies (V_O) have negative formation energies. The simultaneous presence of substitutional Hf and an O vacancy shifts both the VB and CB to higher energies and reduces the band gap, which beneficially reduces the potential of WO_3 for hydrogen evolution in photoactivated water splitting, as shown in **Fig. 14**.

4.2 Alkali metal element doping

Apart from the aforementioned doping elements into the WO_3 structure, it is noteworthy to mention that the alkali metals (Li^+, Na^+, K^+, Cs^+, Rb^+) were theoretically intercalated into the WO_3 interstices as interstitial dopants to examine the changes of the band gap energy, electronic properties and many other physiochemical properties of the structure. For instance, doping alkali metallic elements into the lattice cavities of WO_3 structure induces the formation of tungsten bronzes (M_xWO_3, where M = Na, K, Rb, Cs and etc.), which indicates the influence of electricity as well as the chromogenic properties of alkali metallic dopants. Valentin and co-workers[101] theoretically calculated that the introduction of moderate amounts of alkali metallic cations into the interstices of WO_3 lattice can induce remarkable lattice distortions, reducing the band gap energy of the alkali metallic-doped WO_3. The intercalation of alkali metals into the interstices of the hexagonal WO_3 matrix was also studied using hybrid density functional theory calculations.[102] The structural and electronic properties of mono-doped ($A_{0.083}WO_3$, A = Li, Na, K, Rb, and Cs) and co-doped ($Li_{0.083}A_{0.083}WO_3$, A = Li, Na, K, Rb, and Cs) alkali metals were examined, with both types of dopant shifting the Fermi level of the conduction band upward, leading to metal-like characteristics. These changes result in optical absorption in the visible light and NIR absorption range. Moreover, alkali metal co-doping induces a strong NIR absorption that is not found in a pure hexagonal WO_3. Co-doping is more stable than mono-doping, except in the case of (Li, Li). These alkali metal doped WO_3 studies have paved the way for scientists experimentally realize and apply new, high-performance materials.

4.3 Non-metal element doping

Non-metal doped WO_3 is also a subject of intense materials research focused on tuning its structure and optical and electronic properties. To this end, nitrogen, carbon, sulfur, iodide and tellurium have been used as dopants in the WO_3 lattice. The great achievements in the use of N-doped titanium oxide for visible-light photo-catalytic harvesting have prompted researchers to consider doping N into WO_3 to improve the material performance. Paluselli and co-workers[103] have developed N-doped tungsten oxide films that demonstrate electronic properties different from those of bare intrinsic WO_3 films. They reported that the formation of new electronic states below the conduction band in the N-doped films lowered the band gap energy to as little as 2.2 eV. This work was followed by many other studies, which have provided deep insight into N-doped WO_3. Brian Cole et al.[104] evaluated the change in the band gap energy of WO_3 by doping with N, which significantly impacted its function in photoelectrochemical water splitting. It

was suggested that a high content of N dopants (> 3 mTorr) in the WO_3 lattice can drastically reduce the band gap from 2.5 for pure WO_3 to less than 2.0. However, the doping causes a large decrease in the PEC performance due to the degradation of charge carrier transport as a result of the formation of defects. A similar work[105] reported that nitrogen doped into a WO_3 film via thermal treatment in NH_3 gas provided a visible light region photoresponse. Obviously, nitrogen is a good candidate as a dopant to enhance the visible light harvesting of WO_3. Besides nitrogen, other non-metallic atoms such as S, C, I, and Te[106] have also been intensely studied, providing significant insight into the effect of doping non-metals into the WO_3 lattice on the electronic properties and morphology, as well as the performance of bare WO_3. As a very recent example, Buddie Mullins and co-workers[106a] showed that S and I incorporated into WO_3 result in red shifts of the absorption spectra from ~2.7 to 2.6 and 2.1 eV, respectively. An explanation of the substitution mechanism was reported based on theoretical estimations.

5. WO_3-based heterostructuring

Oxide semiconductors have certain addressable issues, such as limited optical absorption, poor mobility, rapid decay and high recombination of photoexcited carriers. Overcoming such shortcomings is of fundamental importance for industrial applications. Several strategies, including heterostructuring, band gap engineering, morphology tailoring, plasmonic coupling and co-catalyst loading, can be applied to boost the photoactivity.[16b] Band gap tuning allows the optical absorption of the solar spectrum to be extended. A 1D nanostructure provides a direct pathway for electron transfer,[107] and hierarchical structures provide the unique advantages of a larger surface area.[108] Among these, combining two or more materials together is a notable strategy. Integration may be approached in the form of either a nanoscale interface junction formation[109] or a layer-by-layer arrangement[110] backed by solid conducting support. Each route has certain merits and demerits with respect to the ease of fabrication, optoelectronic properties attained and the mode of the final application. Nanoscale heterostructures may improve the optical absorption in different wavelength ranges of the radiation spectrum.[111] They can also potentially contribute to the suppression of the wasteful recombination of photoexcited charge carriers.[112] However, such phenomena are entirely dependent on the intrinsic properties of chosen materials. For instance, the valence and conduction band edges must be located at suitable positions on the electrochemical scale. Electronic synergy driven wasteful recombination can only be suppressed by directing the electrons and holes in opposite directions.

Another important aspect of a heterostructure is the simultaneous exploitation of the combined features of different materials, which is impossible to achieve through the separate use of the individual components. Such a concept has been widely applied in an artificial Z-scheme for overall water splitting.[113] The formation of a heterojunction can also influence the feasibility of photoredox chemistry. It is important to note that photo-driven redox reactions are highly dependent on the oxidation or reduction potential of metal oxides corresponding to the respective valence and conduction band energy levels. Hence, the careful selection of component materials for heterojunction formation is a fundamental consideration. While considering aspects of solution phase synthesis, it is important to mention that the formation of a nanoscale interface junction with controlled morphology is neither straightforward nor easy in all cases. In certain cases, solution phase epitaxy or heterogeneous nucleation and the growth of the second material on the surface of

the first remains quite challenging. Such considerations as crystal lattice matching and reaction condition optimization are indispensable. The use of functional linkers as anchoring agents can facilitate heterogeneous growth.[114] However, their usage also has certain drawbacks in terms of both the additional cost and their potential influence of the charge injection process between materials.[115] Poorly formed interface junctions may act as trapping sites favourable for carrier recombination. Therefore, the quality and area of the interfacial junctions of nanoscale heterostructures must be considered. High-quality interfacial junctions are necessary for optimal recombination suppression and will enable the design of highly efficient photocatalytic materials for various useful applications.

WO_3 has recently been coupled with a variety of other oxides and metals, such as TiO_2,[116] TiO_2/Au,[117] Cu_2O,[118] Fe_2O_3,[119] $B_2O_{33-x}N_x$,[120] Bi_2S_3,[121] CdS,[122] CdS/Au,[123] V_2O_5,[124] $CaFe_2O_4$,[125] C_3N_4,[126] C_3N_4/CoO_x,[127] Si/ITO,[10,128] IrO_2,[129] Bi_2WO_6,[130] $ZnWO_4$,[131] $CuWO_4$,[132] H_2WO_4,[112] $NiWO_4$,[133] $BiVO_4$,[111,134] $BiVO_4/CoPi$,[135] $Fe_2O_3/CoPi$,[136] $BiVO_4/SnO_2$,[137] Al_2O_3,[138] RGO,[139] carbon fibre,[140] PANI,[141] $Cu/PbO_2/Ag$,[142] Ag/CuO,[143] polyoxometalate/Au,[144] Ag,[145] Pt,[146] and Pt/Au.[147] The significance, fabrication, and photocatalytic or photoelectrochemical characteristics of the selected examples are summarized below.
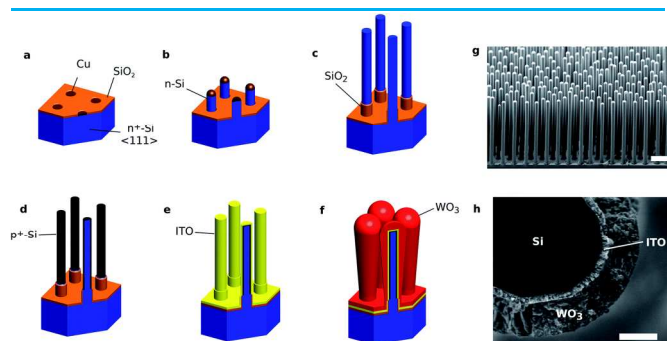
Fig. 15 (a) Photolithographically patterned n^+-Si <111> wafer with a SiO_2 mask layer and Cu catalyst in the desired growth pattern. (b) VLS Cu-catalysed growth of n-type Si microwires on an n^+-Si substrate followed by metal etching (RCA 2). (c) SiO_2 diffusion barrier (boot) formation *via* SiO_2 growth, PDMS infill, HF etch and PDMS removal. (d) p^+-Si emitter drive-in from the BCl_3 precursor at 950 °C for 30 min in a CVD furnace. (e) Conformal DC sputter-coating of ITO. (f) Conformal n-WO_3 electrodeposition and annealing at 400 °C for 2 h. (g) Fully assembled tandem junction device array SEM (scale bar = 10 μm). (h) Cross-sectional SEM of a fully assembled tandem junction single wire demonstrating the layered structure of the device (scale bar = 500 nm). Reproduced from Ref. 128a with permission from the Royal Society of Chemistry.
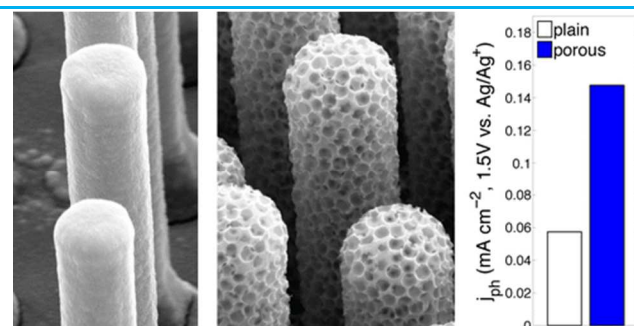
Fig. 16 SEM images of plain and hierarchical structures of Si/WO_3 core-shell tandem photoanodes and their corresponding photocurrents. Reprinted with permission from ref. 128b. Copyright 2014 American Chemical Society.

Silicon (Si) has been explored for PEC H_2 production.[148] However, it suffers certain drawbacks, such as undesired oxidation and insufficient photovoltage generation.[10] Si has been combined with different metal oxides to upgrade its PEC performance.[10,128,149] A WO_3 thin film was electrodeposited on a Si substrate, and the WO_3/Si interface was observed to markedly affect the photocurrent density. Inserting a thin layer of tin-doped indium oxide (ITO) between the WO_3 film and Si substrate resulted in significantly enhanced PEC properties.[10] Unassisted H_2 production has been demonstrated using a Si-based tandem device, with the n-p$^+$-Si nanowires coaxially coated with ITO and WO_3 layers, fabricated as shown in **Fig. 15**. The tandem junction (n-Si/p$^+$-Si/ITO/n-WO_3/1.0 M H_2SO_4) exhibited an E_{oc} of -1.21 V, which is much larger than that of a single junction (p-Si/ITO/n-WO_3/1.0 M H_2SO_4), E_{oc} -0.73 V. Such a shift in E_{oc} has been assigned to the formation of an n-p$^+$-homojunction.[128a] Hierarchical structures have the advantage of a high surface area,[108,150] whereas porosity can improve the charge carrier collection efficiency.[151] Combining the additive features of both may improve PEC performance. A Si/ITO/WO_3 core-shell nanowire-based tandem device has been fabricated, introducing porosity to the outer shell of the WO_3 layer. As a result, a several-order increase in the photocurrent density was observed, as shown in **Fig. 16**.[128b] CdS is a narrow band gap material. It shows absorption in the visible range, a large portion of the solar spectrum. It has been extensively coupled with large band gap materials. The reduction potential of WO_3 is less than that required for H_2 production from water splitting. Hydrothermally prepared WO_3/CdS heterojunctions have exhibited superior H_2 production, nearly five times higher than that of bare CdS. Improved photoactivity was assigned to the effective suppression of carrier recombination. The rate of H_2 production was further improved by the loading of Pt nanoparticles onto a WO_3/CdS heterostructure, which improved the charge transfer process.[122a] One-dimensional nanostructures have unique advantages in terms of their superior electron transfer capability. Vertically aligned 1D WO_3/CdS (core/shell) nanowires were fabricated on W foil using the CVD method. Monoclinic WO_3 nanowire arrays were coated with a hexagonal CdS shell, and the transient photocurrent response indicated significantly improved PEC performance. The coating of the CdS shell resulted in decreased charge transfer resistance, as observed by EIS, as well as an improved lifetime of photoexcited carriers (**Fig. 17**).[122b]
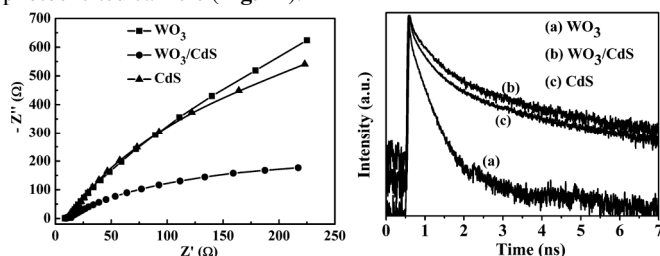

Fig. 17 Nyquist plots of measured EIS spectra (under visible light $\lambda \geq 420$ nm) and photoluminescence decay of pristine WO_3 nanowires, CdS nanowires, and WO_3/CdS core/shell photoelectrodes. Reproduced from Ref. 122b with permission from the Royal Society of Chemistry.

Recently, WO_3/BiVO$_4$ heterojunctions have attracted much attention.[111,134,135,137] J. S Lee and co-workers have demonstrated the polymer-assisted fabrication of WO_3/ BiVO$_4$ films on a FTO substrate in a layer-by-layer arrangement. BiVO$_4$ exhibits better optical absorption, whereas WO_3 provides superior charge transport. Blending the two materials in an appropriate proportion results in higher performance than the use of materials individually. Coating a BiVO$_4$ over-layer on four layers of WO_3 provided the best PEC performance.[134a] Inserting a thin layer of SnO_2 between the WO_3 and the BiVO$_4$ further boosted the PEC characteristics. The increase in

the photocurrent density and IPEC were attributed to the improved interfacial charge transfer capabilities caused by the sandwiched thin layer of SnO_2.[137] Furthermore, WO_3/W-BiVO$_4$ (core/shell) nanowire-based photoanodes have shown excellent PEC performance. WO_3 nanowires were grown on an FTO substrate by flame vapour deposition/annealing. The W-BiVO$_4$ shell was coated by the drop-casting of the BiVO$_4$ precursors followed by thermal annealing. A significant improvement in photocurrent density was observed. Interestingly, the IPCE of this material was found to be the highest among BiVO$_4$-based photoanodes. It was suggested that the PEC performance could be further improved by combining the WO_3/W-BiVO$_4$ photoanode with a suitable OEC catalyst.[111]
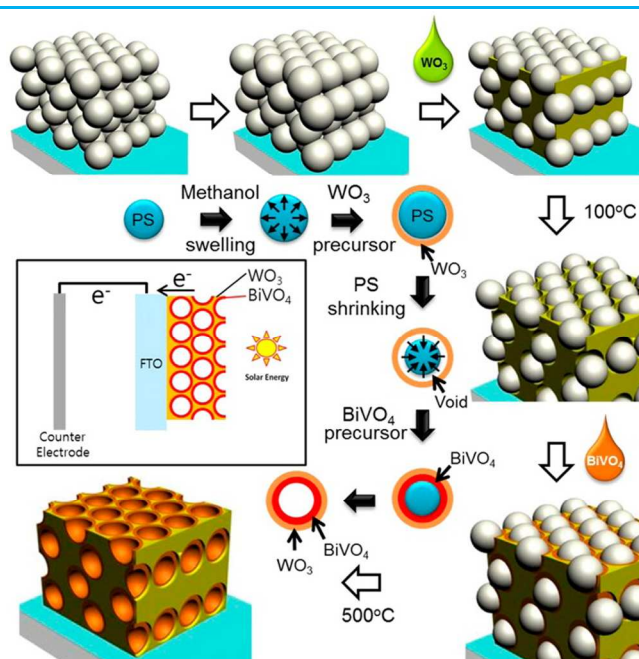
Fig. 18 Schematic diagram of the fabrication procedures for the DDIO-WO_3/BiVO$_4$ photoanodes and PEC cells with DDIO-WO_3/BiVO$_4$ photoanodes. Reprinted with permission from ref. 134b. Copyright 2014 American Chemical Society.

Recently, inverse opal-based periodically ordered photonic crystals have attracted significant attention. Ming Ma and co-workers demonstrated the template-assisted fabrication of a double-deck WO_3/BiVO$_4$ inverse opal photoanode (DDIO-WO_3/BiVO$_4$) using a polystyrene template and a swelling-shrinking approach. DDOI-WO_3/BiVO$_4$ exhibited significantly improved PEC characteristics. The photocurrent density was observed to be 40 times higher than that of a bare WO_3 inverse opal electrode. The larger area of the interfacial junction between WO_3 and BiVO$_4$ is favourable for the effective separation of charge carriers. The scheme for the fabrication of DDOI-WO_3/BiVO$_4$ is shown in **Fig. 18**.[134b] Branched nanowires are generally highly desirable due to their high surface area and efficient charge collection. Pingyun Feng and co-workers[127] demonstrated the fabrication of three-dimensional branched (3DB) WO_3 nanosheet arrays (NA) decorated with C_3N_4 nanosheets (NS) and a CoO$_x$ hybrid photoanode, referred to as 3DB WO_3-NA/C_3N_4//CoO$_x$. The photocurrent density of the hybrid photoanode under 1.5 AG at 2.1 V was observed to be 5.76 mA cm^{-2}, which is 1.88 times higher than that of the bare 3DB WO_3 NA photoanode (3.07 mA cm^{2-}).

Fig. 19 Voltammetric response of transparent Al_2O_3/WO_3 electrodes under simulated AM 1.5G illumination (120 mW cm^{-2}). The alumina over-layer was deposited by ALD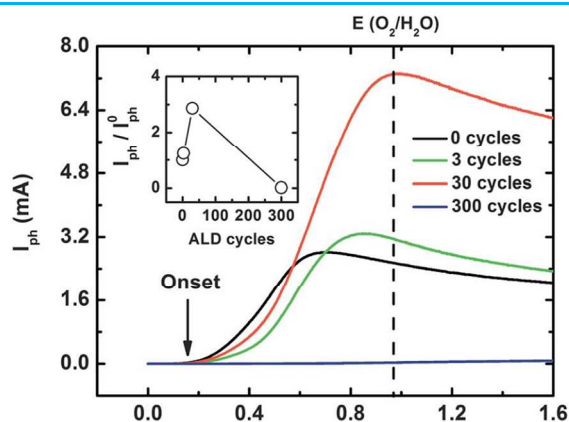 for 0 cycles (black), 3 cycles (green), 30 cycles (red) and 300 cycles (blue). Electrolyte: Ar-purged 0.1 M HClO$_4$ (pH 1.0). Scan rate: 20 mV s^{-1}. The photocurrent (I_{ph}) was obtained by correcting the capacitive contribution in the dark. Inset: normalized photocurrent values taken at 0.97 V vs Ag/AgCl (thermodynamic potential of water oxidation at pH 1.0) as a function of number of ALD cycles. Reproduced from Ref. 138 with permission from the Royal Society of Chemistry.

Atomic layer deposition (ALD) is a versatile technique for depositing atomically thin layers. Adriana Paracchino and co-workers developed ultrathin ALD protective coatings for improved PEC water splitting.[152] Choi and co-workers[138] demonstrated the coating of a very thin Al_2O_3 layer on WO_3. By suppressing the recombination of charge carriers, an alumina over-layer was found to be favourable for water oxidation. The thickness of the alumina layer can be controlled by the number of ALD cycles. Improvement in the photocurrent density was observed to be a function of the number of ALD cycles. As shown in **Fig. 19**, 30 ALD cycles provided an optimized photocurrent response that was three times higher than that of the bare WO_3 electrode.[138] In addition to the formation of WO_3/metal oxide heterojunctions, noble metal coupled WO_3 has also been proven to have enhanced photocatalytic activity. A mesoporous WO_3 film was deposited on a plasmonic AgNP-coated TCO conducting substrate (FTO). The photocurrent and IPCE values were 60% and 50% higher, respectively, than those of a bare WO_3 film. The resonant and non-resonant scattering of light were both suggested to contribute to the improved performance.[145] Because the conduction band edge of WO_3 is more positive than the O_2 reduction potential, it may influence the photodecomposition of organic compounds. By coupling WO_3 with Pt, Ohtani and co-workers[146a] suggested the multi-electron reduction of O_2. Having monitored CO_2 as the degraded product, they demonstrated significantly improved photodecomposition ability under visible irradiation. Very recently, Hiroshi Kominami and co-workers[147] fabricated a Pt/Au/WO_3 photocatalyst and demonstrated the production of H_2 and O_2 in the presence of sacrificial reagents. In explaining the mechanism, they noted that the WO_3 excitation and the SPR of the Au NPs both supported the production of H_2 and O_2. They further suggested that the transfer of Pt/Au/WO_3' electrons from Au to Pt also contributes to favourable H_2 production.[147] Several organic stabilizers or capping agents are often used to improve the stability of plasmonic NPs. Certain inorganic species, such as polyoxometalates (POM), are a potential substitute. Renata Solarska and co-workers[144] demonstrated combining WO_3 with phosphododecamolybdate anion ($PMo_{12}O_{40}^{3-}$) capped plasmonic AuNPs. It was suggested that the catalytic effect of Au-$PMo_{12}O_{40}^{3-}$ and the plasmonic effect of the

AuNPs both contributed to the improved PEC performance. They further suggested that Au-$PMo_{12}O_{40}^{3-}$ supports the separation of charge carriers.[144]

6. Applications

Due to the versatile nature of WO_3 nanoparticles, they have been widely used in various fields. Tungsten oxide is used for many purposes because of its flexibility. The applications of WO_3 are divided into four categories, namely, sensors, catalysts, devices and miscellaneous applications, which can be further classified by use, as shown in **Fig. 20**.
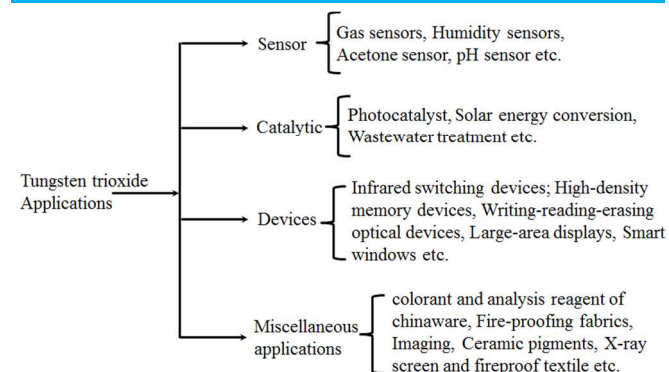

Fig. 20 Schematic representation of the tungsten trioxide applications mentioned in the text.

6.1 Sensors

Many different types of semiconducting metal oxides are well-known for their gas sensing applications, e.g., ZnO, TiO_2, SnO_2, In_2O_3, CuO, CdO, Fe_2O_3, MoO_3, TeO_2 and WO_3. Different metal oxides show different gas sensing properties because of their stoichiometry-dependent conductivity as well as their interstitial anion and cation vacancies.[153] In short, gas sensors work through gas adsorption on the surface, which changes the electrical resistance of the sensor (semiconducting) materials. According to the primary charge carrier type, semiconductors are divided into two categories: n-type and p-type semiconductors. Hence, the detected gas species can also be divided into two groups, electron accepting, or oxidizing, gas species (e.g., NO_2 and O_2) and electron donating, or reducing, gas species (e.g., ethanol, CO, H_2, H_2S and HCHO). Tungsten oxide exhibits n-type semiconducting behaviour; however, it is applicable to both types of gas species (oxidizing and reducing).[154] Among the various applications of WO_3, sensor applications are most common. Therefore, a major portion of the tungsten oxide produced is consumed in the sensor field.

It is well known that sensor performance depends upon several parameters, such as sensitivity, recovery time, response time, working temperature and detection limit. To improve the sensor performance, different material types, sizes and morphologies and different combinations and structure modification processes have been studied. In 1987, the first report of WO_3 as a pH-based sensor was submitted by Wringhton et al.[155] Recently, Santos et al. reported that a WO_3 nanoparticle-based sensor is very effective for pH sensing.[156] It is well known that pH is a vital parameter for disease diagnosis as well as medical treatment. Therefore, to accurately measure the pH, a highly sensitive sensor comprising electrodeposited WO_3 nanoparticles on a flexible metal substrate as an electrode has been prepared. The as-prepared WO_3-based sensor shows a sensitivity of -56.7 ± 1.3 mV/pH over a wide pH range of 9 to 5.

One-dimensional WO_3 has received considerable attention in gas sensing due to its tremendous sensitivity and selectivity performance in detecting different types of gases. One-dimensional WO_3 gas sensors have been frequently chosen for sensing NH_3, H_2S, O_3, NO_2, and H_2 as well as liquefied petroleum gas at high temperatures of approximately 200 – 300 °C.[157] It has been reported that functionalized 1D WO_3-based sensors (specifically, Pt-functionalized WO_3 nanorod based sensors) improve the sensing performance for H_2[158] and CO as well as NO_2 gas.[159] Further modification of 1D WO_3 include 3D mesoporous structures to improve the sensing properties. Qin *et al.* suggested that a mesoporous 3D network of crystalline WO_3 nanowires can exhibit a high sensitivity, good selectivity and fast response–recovery for NO_2 gas sensing applications.[160] The high performance of the mesoporous 3D WO_3 nanowire is a result of its large surface area, perfect single crystallinity and stable mesoporous channels.

Choi *et al.*[161] reported graphene-functionalized hierarchical porous WO_3 nanofibers with 1D nanoneedles for the detection of acetone molecules for the diagnosis of diabetes. The high detection limit of acetone is due to its unique morphology, which creates a high number of reaction sites on the surface of the structure. Righettoni *et al.* reported a Si-doped WO_3 nanoparticle film as an acetone detector for diabetes diagnosis through breath analysis.[162] Tungsten oxide has also been used for the detection of alcohol with porous nanoflakes, and Xiao *et al.* observed that it shows a highly alcohol-sensitive performance.[163]

Another very important application of tungsten trioxide is as a humidity sensor. These humidity sensors are based on through the resistance of the film, which changes with the adsorption or desorption of water vapour.[164] WO_3 composites are most frequently been used as humidity sensors. Bendahan *et al.* reported that a radio frequency (rf) magnetron sputtering deposited WO_3 film on a SiO_2/Si substrate showed a sensor response variation based on the operating temperature.[165] A tungsten oxide composite with an organic material (polyaniline) was also used as a humidity sensor.[166] Recently, Li *et al.*[167] reported a high-temperature humidity sensor with high sensitivity, fast response and long stability that is based on a composite hollow nanosphere structure of WO_3 and SnO_2. The improved properties of the sensor depend upon the composite structure and morphology of the nanoparticles.

6.2 Catalysis

Tungsten oxide has been used in several catalytic applications such as photocatalysis or solar energy conversion, wastewater treatment and RhB degradation. Tungsten trioxide is very well known for its wide band gap energy (~2.6.eV) and absorbs over a long range of visible light, endowing it with many applications in the photocatalytic field. In a study by Tanaka *et al.*[147], a Pt-Au deposited WO_3 photocatalyst drove the reduction and oxidation of H_2 and O_2, respectively, under visible light irradiation. Pt/Au/WO_3 is a new photocatalyst prepared with subsequent colloid photodeposition (CPD). To produce this electrode, Au nanoparticles were initially deposited on WO_3 with photodeposition (PD), and then Pt nanoparticles were deposited on the Au nanoparticles by CPD. The prepared sample continuously produced H_2 and CO_2 through glycerin under a visible light source and O_2 production from water oxidation. The reduction reaction or H_2 formation occurred because of the surface plasmon resonance of the Au nanoparticles, and the valence band position of WO_3 is responsible for the O_2 production. This type of study aids in the design of a new photocatalysts, providing information on SPR (surface plasmon resonance) and band gap excitation.

Tungsten oxide combined with molecular catalysis also improves photocatalytic performance. Generally, molecular catalysis works in the dark and hence requires a sacrificial oxidant (Ce^{4+} or $S_2O_8^{2-}$) to conduct the reaction. Klepser *et al.*[7c] reported that, with the help of an iron molecular catalyst, such as a phosphonate-derivatized complex, Fe(tebppmcn)Cl$_2$, and without any sacrificial oxidant, WO_3 provides a 60% higher water oxidation rate. WO_3 is also used as a reductive catalyst in various applications, such as nitrogen oxide (NO_x) reduction for environmental health issues. Peng *et al.*[168] offered theoretical as well as experimental evidence for the selective catalysis reduction (SCR) of NO_x with NH_3 through a CeO_2-WO_3 catalyst.

Tungsten oxide shows enhanced photocatalytic performance in combination with other materials, such as $NaNbO_3$/WO_3,[169] Ag/CuO/WO_3,[143] WO_3@TiO_2,[170] Bi_2S_3/WO_3[121] and the above-mentioned WO_3-based heterostructuring. Not only does a heterojunction combination of WO_3 show high performance, but a homojunction combination with a minor phase of hydrated tungsten trioxide (WO_3.H_2O) also shows a greatly enhanced photocatalytic performance for the degradation of RhB under visible light.[171] Similarly Qi *et al.*[172] introduced another homojunction combination with different morphologies, such as WO_3 nanorods/nanoparticles/nanoflakes, in a triple layer with a high photocurrent for solar energy conversion. This unique combination has been prepared by a one-step anodization method on a metallic W foil with a longer reaction time. The stability of the prepared triple layer photoanode is enhanced considerably by adding an ultrathin (10 nm) TiO_2 protective layer through ALD.

Liu *et al.* first modified of WO_3 with anionic liquid to increase its photocatalytic performance.[173] In this study, the tungsten trioxide surface is modified by an ionic liquid of [Bmim]I (1-butyl-3-methylimidazolium iodide) using a method of facile impregnation in water at 80 °C. The presence of the positively charged [Bmim]$^+$ bond on the surface effectively hinders the recombination of the photogenerated electron-hole pairs by catching the photoexcited electrons on the conduction band, which could increase the photocatalytic performance. Moreover, [Bmim]I-modified WO_3 shows high stability and long-lasting photocatalytic activity, which is helpful for practical applications. Reyes-Gil *et al.*[116] reported an electrodeposited composite WO_3/TiO_2 nanostructure as a photoanode for water splitting in wastewater treatment. In this study, it is proven that the composite structure improves the solar absorption, photocurrent and photodegradation efficiency of the photoanode compared to the individual WO_3 and TiO_2 photoanodes.

6.3 Devices

Devices are another important application of tungsten trioxide. WO_3 can be used in various devices, such as infrared switching devices, high-density memory devices, writing-reading-erasing optical devices, large-area displays, and smart windows. The electrochromic properties of the material are responsible for these types of applications, enabling it to change optical properties continuously and reversibly with a small electric difference. Tungsten trioxide with different morphologies and in combination with different materials shows improved electrochromic properties, such as crystalline WO_3 nanoparticles,[174] highly porous WO_3,[175] 1D crystalline/amorphous tungsten oxide core/shell heterostructures,[176] WO_3.$2H_2O$ ultrathin nanosheets,[63] 1D WO_3 nano-structures,[177] TiO_2@WO_3 core/shells[178] and hierarchical structure Ti-doped WO_3 films[179].

In 1997, Gavanier *et al.*[92] developed a tungsten trioxide based smart window, motivated by the fact that tungsten trioxide is the most stable electrochromic material. These types of smart windows can change their light transmission properties, such as heat and intensity, with an applied voltage and are also called electrically switchable glasses. Turyan *et al.*[180] reported tungsten oxide films

with "writing-reading-erasing" capabilities using a scanning electrochemical microscope. The writing process produces permanent changes on the surface, but because of the electrochromic properties of WO_3, it can undergo a reversible reduction-oxidation process, which is helpful for fast reading and erasing. Kumar *et al.*[181] also reported a redox-based memory device based on a heterojunction barrier with PT–PPy (polythiophene-polypyrrole) coated indium tin oxide for ion transport. Tungsten oxide can also be used as a nonvolatile memory device upon the deposition of tungsten nanocrystals (WO_3/W nanocrystals) via tungsten silicide by rapid thermal oxidation.[182]

6.4 Miscellaneous applications

Beyond the above applications, WO_3 can also be used as a colorant and analytical reagent for chinaware and in fire-proofing fabrics, ceramic pigments, X-ray screens and fireproof textiles. WO_3 is a rich yellow and is thus also used as a pigment in paints and ceramics.[183]
The composite structure of WO_3 is also useful in various new applications. Wang et al. suggested that WO_3 nanotrees on tungsten foil with 3D V_2O_5 show high performance as a pseudo-capacitor. It is also important for global energy consumption as a significant supercapacitor.[184] It has also been reported that a combination of WO_3 with ZnO can be used as a bright blue phosphor material in vacuum fluorescent displays (VFDs) and field emission displays.[185] Tungsten trioxide is also used as a protective layer on $SrTiO_3$:Pr,Al,Ga phosphor for surface-related degradation in VFDs.[186]

6. Summary and Outlook

This article has summarized the crystal structures and properties of tungsten oxide and its derivatives, such as tungsten suboxides, tungsten trioxide hydrates, tungsten bronzes, and metal tungstates. The {002} facet has the highest surface energy of the three main low index facets, {002}, {020} and {200}. The {111} planes are not the lowest surface energy surfaces, and it is difficult to prepare octahedral WO_3 by a normal reaction. Therefore, the fine-tuning of WO_3 nanoparticles by exposing specific facets, especially {002} and {111}, is highlighted. Unlike TiO_2 and $BiVO_4$, the properties of different facets of WO_3 remain unclear. Syntheses of uniform WO_3 crystals with different clear facets should be developed in the future. WO_3 films with dominant orientations, along {002}, are summarized. It is difficult to unambiguously assign the good photocurrents resulting from the orientation of the nanoparticles because the photoelectrochemical activity can be influenced by many other factors, such as the surface area, porosity or thickness of the film. More related work should be conducted to show that the oriented films have better properties, such as photoelectrochemical properties. The doping of WO_3, WO_3-based heterostructuring and the applications of WO_3 are also summarized. The doping of various elemental dopants into the WO_3 structure have been intensively attempted by many researchers to improve its activity and physicochemical properties. The as-doped WO_3 materials undergo great changes in their intrinsic behaviours with the addition of dopant impurities. To this end, new materials with high application potential can be fabricated. However, the doping of metal oxides is still a contentious subject in the literature, and this paper aims to highlight the essential understandings of the doping of WO_3. High-quality interfacial junctions will be helpful for electron-hole recombination suppression in photoelectron/photochemical systems. Ultimately, this will also be favourable for the design of highly efficient photocatalytic

materials for various useful applications. The best photocatalytic properties of WO_3 are obtained from optimized heterostructuring. There is still significant room for enhancing the capabilities of these applications through the fine-tuning of the nanostructures of tungsten oxides. The scope of application can be expanded to drug delivery and sensors in microfluidic systems.[19] We expect more potential applications of tungsten oxides to be commercialized in the future.

Notes and references

Korea Center for Artificial Photosynthesis, Department of Chemistry, Sogang University, Seoul 121-742, South Korea. Tel.: +82-2-705-8882; Fax: +82-2-701-0967; Email: yskang@sogang.ac.kr

1   L. Jing, W. Zhou, G. Tian and H. Fu, *Chem. Soc. Rev.*, 2013, **42**, 9509.
2   A. Fujishima and K. Honda, *Nature*, 1972, **238**, 37.
3   M. A. Butler, *J. Appl. Phys.*, 1977, **48**, 1914– 1920.
4   (a) J. H. Kennedy and K. W. Jr. Frese, *J. Electrochem. Soc.*, 1978, **125**, 709; (b) M. A. Butler, *J. Appl. Phys.*, 1977, **48**, 1914.
5   F. Wang, C. D. Valentin and G. Pacchioni, *J. Phys. Chem. C*, 2012, **116**, 8901.
6   (a) G. R. Bamwenda and H. Arakawa, *Appl. Catal.*, A, 2001, **210**, 181; (b) J. Y. Zheng, G. Song, C. W. Kim and Y. S. Kang, *Electrochim. Acta*, 2012, **69**, 340. (c) J. Qiao, Y. Liu, F. Hong and J. Zhang, *Chem. Soc. Rev.*, 2014, **43**, 631.
7   (a) T. Hisatomi , J. Kubota and K. Domen, *Chem. Soc. Rev.*, 2014, **43**, 7520; (b) M. Ni, M. K. H. Leung, D. Y. C. Leung and K. Sumathy, *Renew. Sust. Energy Rev.*, 2007, **11**, 401; (c) B. M. Klepser and B. M. Bartlett, *J. Am. Chem. Soc.*, 2014, **136**, 1694; (d) D. J. Martin, P. J. T. Reardon, S. J. A. Moniz and J. Tang, *J. Am. Chem. Soc.*, 2014, **136**, 12568.
8   H. Wang, T. Deutsch and J. A. Turner, *J. Electrochem. Soc.*, 2008, **155**, F91-F96.
9   Q. P. Chen, J. H. Li, X. J. Li, K. Huang, B. X. Zhou, W. M. Cai and W. F. Shangguan, *Environ. Sci. Technol.*, 2012, **46**, 11451.
10   R. H. Coridan, M. Shaner, C. Wiggenhorn, B. S. Brunschwig and N. S. Lewis, *J. Phys. Chem. C*, 2013, **117**, 6949.
11   Z. F. Huang, L. Pan, J. J. Zou, X. W. Zhang and L. Wang, *Nanoscale*, 2014, **6**, 14044.
12   M. S. Prevot and K. Sivula, *J. Phys. Chem. C*, 2013, **117**, 17879.
13   J. Li and N. Wu, *Catal. Sci. Technol.*, 2015, **5**, 1360.
14   R. Solarska, B. D. Alexander, A. Braun, R. Jurczakowski, G. Fortunato, M. Stiefel, T. Graule and J. Augustynski, *Electrochim. Acta*, 2010, **55**, 7780.
15   J. Brillet, J. Yum, M. Cornuz, T. Hisatomi, R. Solarska, J. Augustynski, M. Graetzel and K. Sivula, *Nat. Photonics*, 2012, **6**, 824.
16   (a) X. Liu, F. Wang and Q. Wang, *Phys. Chem. Chem. Phys.*, 2012, **14**, 7894; (b) F. E. Osterloh, *Chem. Soc. Rev.*, 2013, **42**, 2294; (c) C. A. Bignozzi, S. Caramori, V. Cristino, R. Argazzi, L. Meda and A. Tacca, *Chem. Soc. Rev.*, 2013, **42**, 2228; (d) T. Zhu, M. N. Chong and E. S. Chan, *ChemSusChem*, 2014, **7**, 2974.
17   M. D. Bhatt and J. S. Lee, *J. Mater. Chem. A*, 2015, DOI: 10.1039/C5TA00257E.
18   (a) T. Guo, M.-S. Yao, Y.-H. Lin and C.-W. Nan, *CrystEngComm*, 2015, **17**, 3551; (b) H. Long, W. Zeng and H. Zhang, *J. Mater. Sci. Mater. Electron.*, 2015, DOI:10.1007/s10854-015-2896-4.
19   H. D. Zheng, J. Z. Ou, M. S. Strano, R. B. Kaner, A. Mitchell and K. Kalantar-Zadeh, *Adv. Funct. Mater.*, 2011, **21**, 2175.
20   E. Salje, *Acta Crystallogr.*, 1977, **B33**, 574.
21   J. Y. Zheng, G. Song, J. Hong, T. K. Van, A. U. Pawar, D. Y. Kim, C. W. Kim, Z. Haider and Y. S. Kang, *Cryst. Growth Des.*, 2014, **14**, 6057.

22 B. Gerand, G. Nowogrocki, J. Guenot and M. Figlarz, *J. Solid State Chem.*, 1979, **29**, 429.

23 (a) A. Z. Sadek, H. D. Zheng, K. Latham, W. Wlodarski and K. Kalantar-Zadeh, *Langmuir*, 2009, **25**, 509; (b) C. Ng, C. H. Ye, Y. H. Ng and R. Amal, *Cryst. Growth Des.*, 2010, **10**, 3794; (c) M. Yang, N. K. Shrestha and P. Schmuki, *Electrochem. Commun.*, 2009, **11**, 1908.

24 Y. Guo, N. Murata, K. Ono and T. Okazaki, *J. Nanopart. Res.*, 2005, **7**, 101.

25 (a) P. Gadó, *Acta Phys. Hung.*, 1965, **18**, 111; (b) J. Chen, D. Lu, W. Zhang, F. Xie, J. Zhou, L. Gong, X. Liu, S. Deng and N. Xu, *J. Phys. D: Appl. Phys.*, 2008, **41**, 115305.; (c) F. Galléa, Z. Li and Z. Zhang, *Appl. Phys. Lett.*, 2006, **89**, 193111.

26 (a) M. Remškar, J. Kovac, M. Viršek, M. Mrak, A. Jesih and A. Seabaugh, *Adv. Funct. Mater.*, 2007, **17**, 1974; (b) M. Zumer, V. Nemanič, B. Zajec, M. Wang, J. Wang, Y. Liu and L.-M. Peng, *J. Phys. Chem. C*, 2008, **112**, 5250.

27 (a) B. J.-W. Liu, J. Zheng, J.-L. Wang, J. Xu, H.-H. Li and S.-H. Yu, *Nano Lett.*, 2013, **13**, 3589; (b) G. Gu, B. Zheng, W. Q. Han, S. Roth and J. Liu, *Nano Lett.*, 2002, **2**, 849; (c) C. Guo, S. Yin, M. Yan, M. Kobayashi, M. Kakihana and T. Sato, *Inorg. Chem.*, 2012, **51**, 4763; (d) F. Liu, F. Y. Mo, S. Y. Jin, L. Li, Z. S. Chen, R. Sun, J. Chen, S. Z. Deng and N. S. Xu, *Nanoscale*, 2011, **3**, 1850.

28 (a) X. Huang, H.-J. Zhai, J. L. and L.-S. Wang, *J. Phys. Chem. A*, 2006, **110**, 85; (b) R. Hu, H. Wu and K. Hong, *J. Cryst. Growth*, 2007, **306**, 395.

29 W. Hu, Y. Zhu, W. Hsu, B. Chang, M. Terrones, N. Grobert, H. Terrones, J. Hare, H. Kroto and D. Walton, *Appl. Phys. A: Mater. Sci. Process.*, 2000, **70**, 231.

30 (a) Y.-R. Ma, C.-M. Lin, C.-L. Yeh and R.-T. Huang, *J. Vac. Sci. Technol., B*, 2005, 23, 2141; (b) F. Liu, L. Li, F. Mo, J. Chen, S. Deng and N. Xu, *Cryst. Growth Des.*, 2010, **10**, 5193.

31 (a) D. Davazoglou, A. Moutsakis, V. Valamontes and V. Psycharis, *J. Electrochem. Soc.*, 1997, **144**, 595; (b) D. Davazoglou and K. Georgouleas, *J. Electrochem. Soc.*, 1998, **145**, 1346; (c) S. Ashraf, C. S. Blackman, R. G. Palgrave, S. C. Naisbitt and I. P. Parkin, *J. Mater. Chem.*, 2007, **17**, 3708–3713.

32 P. A. Williams, P. Leverett, J. L. Sharpe, D. M. Colchester, *Can. Mineral.*, 2005, **43**, 1061-1064.

33 B. Gerand, G. Nowogrocki, G. and M. Figlarz, *J. Solid State Chem.*, 1981, **38**, 312-320.

34 (a) R. Nedjar, M. M. Borel, M. Raveau and B. Hervieu, *Mat. Res. Bull.*, 1988, **23**, 91; (b) J. R. Günter, M. Amberg and H. Schmalle, *Materials Res. Bull.*, 1989, **24**, 289.

35 J. T. Szymanski and A. C. Roberts, *Can. Mineral.*, 1984, **22**, 681.

36 (a) M. L. Freedman, *J. Am. Chem. Soc.*, 1959, **81**, 3834; (b) M. L. Freedman, S. Leber, . *J. Less-Common Met.* 1964, **7**, 427.

37 A. Chemseddine, F. Babonneau and J. Livage, *J. Non-Cryst. Solids*, 1987, **91**, 271.

38 (a) C.H. Ruscher, K.R. Dey, T. Debnath, I. Horn, R. Glaum and A. Hussain, *J. Solid State Chem.*, 2008, **181**, 90; (b) E. Masettib, D. Dinia and F. Deckera, *Sol. Energy Mater. Sol. Cells*, 1995, **39**, 310; (c) S. Yue and Y. Zhang, *J. Mater. Sci. Technol.*, 2012, **28**, 569; (d) Z. Gu, Y. Ma, T. Zhai, B. Gao, W. Yang and J. Yao, *Chem. Eur. J.*, 2006, **12**, 7717; (e) R. Brusetti, P. Bordet and J. Marcus, *J. Solid State Chem.*, 2003, **172**, 148; (f) Z. Barkay, E. Grunbaum, G. Leitus and S. Reich, *J. Supercond. Nov. Magn.*, 2008, **21**, 145; (g) J. X. Liu, F. Shi, X. L. Dong, S. H. Liu, C. Y. Fan, S. Yin and T. Sato, *Powder Technol.*, 2015, **270**, 329; (h) L. Kang, W. Xu, K. Wang, W. Liang, X. Liu, F. Gao, A. Lan, Y. Yang and Y. Gao, *Sol. Energy Mater. Sol. Cells*, 2014, **128**, 184; (i)Y. Liu, L. Zhao, J. Su, M. Li and L. Guo, *ACS Appl. Mater. Interface*s, 2015, **7**, 3532.

39 I. M. Szilágyi, J. Madarász, G. Pokol, P. Király, G. Tárkányi, S. Saukko, J. Mizsei, A. L. Tóth, A. Szabó and K. Varga-Josepovits, *Chem. Mater.*, 2008, **20**, 4116.

40 (a) A. Erb and J. C. Lanfranchi, *CrystEngComm*, 2013, **15**, 2301-2304; (b) L. S. Cavalcante, V. M. Longo, J. C. Sczancoski, M. A. P. Almeida, A. A. Batista, J. A. Varela, M. O. Orlandi, E. Longo and M. Siu Li, *CrystEngComm*, 2012, **14**, 853.

41 (a) Y.-X. Zhou, H.-B. Yao, Q. Zhang, J.-Y. Gong, S.-J. Liu and S.-H. Yu, *Inorg. Chem.*, 2009, **48**, 1082; (b) C. Gong, Y.-J. Bai, J. Feng, R. Tang, Y.-X. Qi, N. Lun and R.-H. Fan, *ACS Appl. Mater. Interfaces*, 2013, **5**, 4209; (c) X. Cao, Y. Chen, S. Jiao, Z. Fang, M. Xu, X. Liu, L. Li, G. Pang and S. Feng, *Nanoscale*, 2014, **6**, 12366.

42 (a) J. Deng, L. Chang, P. Wang, E. Zhang, J. Ma and T. Wang, *Cryst. Res. Technol.*, 2012, **47**, 1004; (b) B. Sun , H. Li, L. Wei and P. Chen, *CrystEngComm*, 2014, **16**, 9891.

43 (a) Y. Bi, H. Nie, D. Li, S. Zeng, Q. Yang and M. Li, *Chem. Commun.*, 2010, **46**, 7430; (b) B. Sun, W. Zhao, L. Wei, H. Li and P. Chen, *Chem. Commun.*, 2014, **50**, 13142.

44 (a) J. E. Yourey and B. M. Bartlett, *J. Mater. Chem.*, 2011, **21**, 7651; (b) J. E. Yourey , K. J. Pyper , J. B. Kurtz , and B. M. Bartlett, *J. Phys. Chem. C*, 2013, **117**, 8708.

45 C. Zhang, H. Zhang, K. Zhang, X. Li, Q. Leng and C. Hu, *ACS Appl. Mater. Interfaces*, 2014, **6**, 14423.

46 (a) Y. Zhou, Z. Tian, Z. Zhao, Q. Liu, J. Kou, X. Chen, J. Gao, S. Yan and Z. Zou, *ACS Appl. Mater. Interfaces*, 2011, **3**, 3594; (b) H. Cheng, B. Huang, Y. Liu, Z. Wang, X. Qin, X. Zhang and Y. Dai, *Chem. Commun.*, 2012, **48**, 9729; (c) S. Murcia-López, V. Vaiano, M. C. Hidalgo, J. A. Navío and D. Sannino, *Photochem. Photobiol. Sci.*, 2015, **14**, 678; (d) Y. Zhang, N. Zhang, Z.-R. Tang and Y.-J. Xu, Chem. Sci., 2013, **4**, 1820; (e) T. Saison, P. Gras, N. Chemin, C. Chanéac, O. Duruphty, V. Brezová, C. Colbeau-Justin and J.-P. Jolivet, *J. Phys. Chem. C*, 2013, **117**, 22656; (f) N. Zhang, R. Ciriminna, M. Pagliaro and Y.-J. Xu, *Chem. Soc. Rev.*, 2014, **43**, 5276.

47 M.V. Korzhik, V.B. Pavlenko and V.A. Katchanov, J.-P. Peigneux and M. Poulet. *MRS Proc.*, 1994, **348**, 285.

48 I. Aslam, C. Cao, M. Tanveer, M. H. Farooq, W. S. Khan, M. Tahir, F. Idreesa and S. Khalid, *RSC Adv.*, 2015, **5**, 6019.

49 S. Murcia-López, K. Villa, T. Andreu and J. R. Morante, *ACS Catal.*, 2014, **4**, 3013.

50 (a) J. Kukkola, M. Mohl, A.-R. Leino, G. Tóth, M.-C. Wu, A. Shchukarev, A. Popov, J.-P. Mikkola, J. Lauri, M. Riihimäki, J. Lappalainen, H. Jantunen and K. Kordás, *J. Mater. Chem.*, 2012, **22**, 17878; (b) L. Santos, P. Wojcik, J. V. Pinto, E. Elangovan, J. Viegas, L. Pereira, R. Martins and E. Fortunato, *Adv. Electron. Mater.*, 2015, **1**, 1400002.

51 J. Y. Zheng, G. Song, C. W. Kim and Y. S. Kang, *Nanoscale*, 2013, **5**, 5279.

52 W. Tu, Y. Zhou, Z. Zou, *Adv. Mater.* 2014, **26**, 4607.

53 (a) G. Liu, J. Yu, G. Q. Lu and H.-M. Cheng, *Chem. Commun.*, 2011, **47**, 6763; (b) G. Liu, H. G. Yang, J. Pan, Y. Q. Yang, G. Q. Lu and H.-M. Chen, *Chem. Rev.*, 2014, **114**, 9559.

54 (a) R. G. Li, F. X. Zhang, D. E. Wang, J. X. Yang, M. R. Li, J. Zhu, X. Zhou, H. X. Han and C. Li, *Nat. Commun.*, 2013, **4**, 1432; (b) R. Li, H. Han, F. Zhang, D. Wang and C. Li, *Energy Environ. Sci.*, 2014, **7**, 1369; (c) C. Li, P. Zhang, R. Lv, J. Lu, T. Wang, S. Wang, H. Wang and J. Gong, *Small*, 2013, **9**, 3951.

55 Y. Guo, X. Quan, N. Lu, H. Zhao and A. S. Chen, *Environ. Sci. Technol.* 2007, **41**, 4422.

56 Á. Valdés and G.-J. Kroes, *J. Chem. Phys.*, 2009, **130**, 114701.

57 Y. P. Xie, G. Liu, L. Yin and H. M. Chen, *J. Mater. Chem.*, 2012, **22**, 6746.

58 X. Chen, Y. Zhou, Q. Liu, Z. Li, J. Liu and Z. Zou, *ACS Appl. Mater. Interfaces*, 2012, **4**, 3372.

59 X. Han, X. Han, L. Li and C. Wang, *New J. Chem.*, 2012, **36**, 2205.

60 H. Zhang, J. Yang, D. Li, W. Guo, Q. Qin, L. Zhu and W. Zheng, *Appl. Surf. Sci.*, 2014, **305**, 274.

61 J. Ma, J. Zhang, S. Wang, T. Wang, J. Lian, X. Duan and W. Zheng, *J. Phys. Chem. C*, 2011, **115**, 18157.

62 L. Zhou, J. Zou, M. Yu, P. Lu, J. Wei, Y. Qian, Y. Wang and C. Yu, *Cryst. Growth Des.*, 2008, **8**, 3993.

63 L. Liang, J. Zhang, Y. Zhou, J. Xie, X. Zhang, M. Guan, B. Pan and Yi Xie, *Sci. Rep.*, 2013, **3**, 1936.

64 B. Miao, W. Zeng, S. Xu, S. Zeng, Y. Chen and S. Wu, *Mater. Lett.*, 2013, **113**, 13.

65 M. Ahmadia and M. J.-F. Guine, *Acta Mater.*, 2014, **69**, 203.

66 J. Yang, W. Li, J. Li, D. Sun and Q. Chen, *J. Mater. Chem.*, 2012, **22**, 17744.

67 D.-L. Chen, L. Gao, A. Yasumori, K. Kuroda and Y. Sugahara, *Small*, 2008, **4**, 1813.

68 (a) Z. G. Zhao, Z. F. Liu and M. Miyauchi, *Chem. Commun.* 2010, **46**, 3321; (b) A. Sonia, Y. Djaoued, B. Subramanian, R. Jacques, M. Eric, B. Ralf and B. Achour, *Mater. Chem. Phys.*, 2012, **136**, 80; (c) H. Zhang, H. Yao, M. Bai, L. Xiang, H. Jin, J. Li and F. Yuan, *CrystEngComm*, 2013,**15**, 1432; (d) M. Yao, Q. Li, G. Hou, C. Lu, B. Cheng, K. Wu, G. Xu, F. Yuan, F. Ding and Y. Chen, *ACS Appl. Mater.*

Interfaces, 2015, **7**, 2856; (e) J. Shi , G. Hu, R. Cong, H. Bu and N. Dai, *New J. Chem.*, 2013, **37**, 1538; (f) I. Aslam, C. Cao, W. S. Khan, M. Tanveer, M. Abid, F. Idrees, R. Riasat, M. Tahir, F. K. Butt and Z. Ali, *RSC Adv.*, 2014, **4**, 37914; (g) X. Chang, S. Sun, L. Dong, Y. Dong and Y. Yin, *RSC Adv.*, 2014, **4**, 8994; (h) H. W. Long, W. Zeng, Y. Q. Li, W. G. Chen, B. Miao and C. X. Wang, *Nanosci. Nanotechnol. Lett.*, 2014, **6**, 1.

69   M. Nespolo and G. Ferraris, *Eur. J. Mineral.*, 2004, **16**, 401.

70   (a) Z. J. Gu, T. Y. Zhai, B. F. Gao, X. H. Sheng, Y. B. Wang, H. B. Fu, Y. Ma and J. N. Yao, *J. Phys. Chem. B*, 2006, **110**, 23829; (b) Z. J. Gu, Y. Ma, W. S. Yang, G. J. Zhang and J. N. Yao, *Chem. Commun.*, 2005, 3597; (c) X. C. Song, Y. F. Zheng, E. Yang and Y. Wang, *Mater. Lett.* 2007, **61**, 3904; (d) J. Li, X. Liu, Q. Han, X.Yao and X. Wang, *J. Mater. Chem. A*, 2013, **1**, 1246.

71   (a) Y. Kobayashi, S. Terada and K. Kubota, *Thin Solid Films*, 1989, **168**, 133; (b) L. J. LeGore, O. D. Greenwood, J. W. Paulus, D. J. Frankel and R. J. Lad, *J. Vac. Sci. Technol.*, A, 1997, **15**, 1223; (c) A. Garg, J. A. Leake and Z. H. Barber, *J. Phys. D: Appl. Phys.*, 2000, **33**, 1048.

72   P. Tagtstrom and U. Jansson, *Thin Solid Films*, 1999, **352**, 107.

73   M. J. Wang, G. J. Fang, L. Y. Yuan, H. H. Huang, Z. H. Sun, N. S. Liu, S. H. Xia and X. Z. Zhao, *Nanotechnology*, 2009, **20**, 185304.

74   S. Ling, D. Mei and M. Gutowski, *Catal. Today*, 2011, **165**, 41.

75   C. Santato, M. Odziemkowski, M. Ulmann and J. Augustynski, *J. Am. Chem. Soc.*, 2001, **123**, 10639.

76   R. Liu, Y. Lin, L.-Y. Chou, S. W. Sheehan, W. He, F. Zhang, H. J. M. Hou and D. Wang, *Angew. Chem.*, 2011, **123**, 519.

77   P. J. Wojcik, A. S. Cruz, L. Santos, L. Pereira, R. Martins, E. Fortunato, *J. Mater. Chem.*, 2012, **22**, 13268.

78   A. A. Mohammad, *Vacuum*, 2009, **83**, 1326.

79   S. Yamamoto, A. Inouye and M. Yoshikawa, *Nucl. Instrum. Methods B*, 2008, **266**, 802.

80   R. Solarska, R. Jurczakowski and J. Augustynski, *Nanoscale*, 2012, **4**, 1553.

81   W. L. Kwong, N. Savvides and C. C. Sorrell, *Electrochim. Acta*, 2012, **75**, 371.

82   S. Hilaire, M. J. Suess, N. Kranzlin, K. Bienkowski, R. Solarska, J. Augustynski and M. Niederberger, *J. Mater. Chem. A*, 2014, **2**, 20530.

83   S. Emin, M. de Respinis, M. Fanetti, W. Smith, M. valant and B. Dam, *Appl. Catal. B: Environ.*, 2015, **166-167**, 406.

84   (a) J. S. Lee, J. H. Kim, Y. J. Lee, N. C. Jeong and K. B. Yoon, *Angew. Chem. Int. Ed.*, 2007, **46**, 3087; (b) N. N. Khanh and K. B. Yoon, *J. Am. Chem. Soc.*, 2009, **131**, 14228; (c) T. C. T. Pham, H. S. Kim and K. B. Yoon, *Science*, 2011, **334**, 1553; (d) T. K. Van, C. K. Nguyen and Y. S. Kang, *Chem.-Eur. J.*, 2013, **19**, 9376.

85   (a) A. Kudo and Y. Meseki, *Chem. Soc. Rev.*, 2009, **38**, 253; (b) J. Barber, *Chem. Soc. Rev.*, 2009, **38**, 185; (c) X. Chen, S. Shen, L. Guo and S. S. Mao, *Chem. Rev.*, 2010, **110**, 6503.

86   S. N. Habisreutinger, L. Schmidt-Mende and J. K. Stolarczyk, *Angew. Chem. Int. Ed.*, 2013, **52**, 7372.

87   A. A. Krasnovsky and G. P. Brin, *Dokl. Akad. Nauk SSSR*, 1962, **147**, 656.

88   P. Maruthamuthu, M. Ashokkumar, K. Gurunathan, E. Subramanian and M. V. C. Sastri, *Int. J. Hydrogen Energy*, 1989, **14**, 525.

89   A. Hameed, M.A. Gondal and Z.H. Yamani, *Catal. Commun.*, 2004, **5**, 715.

90   M. Radecka, P. Sobas, M. Wierzbicka and M. Rekas, *Physica B*, 2005, **364**, 85.

91   C. Feng, S. Wang and B. Geng, *Nanoscale*, 2011, 3, 3695.

92   G. -F. Cai, X. -L. Wang, D. Zhou, J. H. Zhang, Q. Q. Xiong, C. D. Gu and J. -P. Tu, *RSC Adv.*, 2013, **3**, 6896.

93   K. M. Karuppasamy and A. Subrahmanyam, *J. Phys. D: Appl. Phys.*, 2008, **41**, 035302.

94   X. F. Cheng, W.H. Leng, D. P. Liu, J. Q. Zhang and C. N. Cao, *Chemosphere*, 2007, **68**, 1976.

95   A. Enesca, A. Duta, and J. Schoonman, *Phys. Stat. Sol. (a)*, 2008, **205**, 2038.

96   X. C. Song, E. Yang, G. Liu, Y. Zhang, Z. S. Liu, H. F. Chen and Y. Wang, *J. Nanopart. Res.*, 2010, **12**, 2813.

97   L. Zhou, J. Zhu, M. Yu, X. Huang, Z. Li, Y. Wang and C. Yu, *J. Phys. Chem. C*, 2010, **114**, 20947.

98   X. Chang, S. Sun,Y. Zhou, L. Dong and Y. Yin, *Nanotechnology*, 2011, **22**, 265603.

99   H. Liu, T. Peng, D. Ke, Z. Peng and C. Yan, *Mater. Chem. Phys.*, 2007, **104**, 377.

100 F. Wang, C. D. Valentin and G. Pacchioni, *ChemCatChem*, 2012, **4**, 476.

101 S. Tosoni, C. D. Valentin and G. Pacchioni, *J. Phys. Chem. C*, 2014, **118**, 3000.

102 C. Yang, J. -F. Chen, X. Zeng, D. Cheng, and D. Cao, *Ind. Eng. Chem. Res.*, 2014, **53**, 17981.

103 D. Paluselli, B. Marsen, E. L. Miller, and R. E. Rocheleau, *Electrochem. Solid-State Lett.*, 2005, **8**, G301.

104 B. Cole, B. Marsen, E. Miller, Y. Yan, B. To, K. Jones, and M. Al-Jassim, *J. Phys. Chem. C*, 2008, **112**, 5213.

105 Y. -C. Nah, I. Paramasivam, R. Hahn, N. K Shrestha and P. Schmuki, *Nanotechnology*, 2010, **21**, 105704.

106 (a) A. J. E. Rettie, K. C. Klavetter, J. –F. Lin, A. Dolocan, H. Celio, A. Ishiekwene, H. L. Bolton, K. N. Pearson, N. T. Hahn, and C. B. Mullins, *Chem. Mater.*, 2014, **26**, 1670; (b) Y. Sun, C. J. Murphy, K. R. Reyes-Gil, E. A. Reyes-Garcia, J. M. Thornton, N. A. Morris, D. Raftery, *Int. J. Hydrogen Energy*, 2009, **34**, 8476; (c) B. Yang and V. Luca, *Chem. Commun.*, 2008, 4454.

107 D. R. Baker, P. V. Kamat, *Adv. Funct. Mater.*, 2009, **19**, 805.

108 Z. Haider and Y. Soo Kang, *ACS Appl. Mater. Interfaces*, 2014, **6**, 10342.

109 S. Li, J. Cai, X. Wu, F. Zheng, X. Lin, W. Liang, J. Chen, J. Zheng, Z. Lai, T. Chen and L. Zhu, *Appl. Catal. B: Environ.*, 2014, **160–161**, 279.

110 A. O. T. Patrocinio, L. F. Paula, R. M. Paniago, J. Freitag and D. W. Bahnemann, *ACS Appl. Mater. Interfaces*, 2014, **6**, 16859.

111 P. M. Rao, L. Cai, C. Liu, I. S. Cho, C. H. Lee, J. M. Weisse, P. Yang and X. Zheng, *Nano Lett.*, 2014, **14**, 1099.

112 J. Cao, B. Luo, H. Lin, B. Xu and S. Chen, *Appl. Catal. B:Environ.*, 2012, **111– 112**, 288.

113 K. Maeda, *ACS Catal.*, 2013, **3**, 1486.

114 K. Mori, K. Watanabe, K. Fuku and H. Yamashita, *Chem. Eur. J.*, 2012, **18**, 415.

115 S. Ardo and G. J. Meyer, *Chem. Soc. Rev.*, 2009, **38**, 115.

116 K. R. Reyes-Gil and D.B. Robinson, *ACS Appl. Mater. Interfaces*, 2013, **5**, 12400.

117 (a) G. Kovacsa, L. Baiaa, A. Vulpoia, T. Radu, E. Karacsonyi, A. Dombi, K. Hernadi, V. Danciu, S. Simon and Zs. Pap, *Appl. Catal. B: Environ.*, 2014, **147**, 508; (b) L. Baia, A. Vulpoi, T. Radu, E. Karacsonyi, A. Dombi, K. Hernadi, V. Danciu, S. Simon, K. Noren, S.E. Canton, G. Kovacs and Zs. Pap, *Appl. Catal. B: Environ.*, 2014, **148–149**, 589.

118 A. M. Garcia, V. K. Vendra, S. Sunkara, P. Haldankar, J. Jasinski and M. K. Sunkara, *J. Mater. Chem. A*, 2013, **1**, 15235.

119 S. Bai, K. Zhang, J. Sun, R. Luo, D. Li and A. Chen, *CrystEngComm*, 2014, **16**, 3289.

120 Y. P. Xie, G. Liu, G. Q. M. Lu and H. M. Cheng, *Nanoscale*, 2012, **4**, 1267.

121 H. He, S. P. Berglund, P. Xiao, W. D. Chemelewski, Y. Zhang and C. B. Mullins, *J. Mater. Chem. A*, 2013, **1**, 12826.

122 (a) L. J. Zhang, S. Li, B. Liu, D. J. Wang and T. Xie. *ACS Catal.*, 2014, **4**, 3724; (b) H. Li, Y. Zhou, L. Chen, W. Luo, Q. Xu, X. Wang, M. Xiao and Z. Zou, *Nanoscale*, 2013, **5**, 11933.

123 X. Cui, Y. Wang, G. Jiang, Z. Zhao, C. Xu, Y. Wei, A. Duan, J. Liu and J. Gao, *RSC Adv.*, 2014, **4**, 15689.

124 E. Skliri, I. N. Lykakis and G. S. Armatas, *RSC Adv.*, 2014, **4**, 46170.

125 M. Miyauchi, Y. Nukui, D. Atarashi and E. Sakai, *ACS Appl. Mater. Interfaces*, 2013, **5**, 9770.

126 H. Katsumata, Y. Tachi, T. Suzuki and S. Kaneco, *RSC Adv.*, 2014, **4**, 21405.

127 Y. Hou , F. Zuo , A. P. Dagg , J. Liu and P. Feng, *Adv. Mater.*, 2014, **26**, 5043.

128 (a) M. R. Shaner, K. T. Fountaine, S. Ardo, R. H. Coridan, H. A. Atwater and N. S. Lewis. *Energy Environ. Sci.*, 2014, **7**, 779; (b) R.H. Coridan, K. A. Arpin, B. S. Brunschwig, P. V. Braun and N. S. Lewis, *Nano Lett.*, 2014, **14**, 2310.

129 J. M. Spurgeon, J. M. Velazquez and M. T. McDowell, *Phys. Chem. Chem. Phys.*, 2014, **16**, 3623.

130 (a) Y. Peng, Q. G. Chen, D. Wang, H.Y. Zhou and A. W. Xu, *CrystEngComm*, 2015 , **17**, 569; (b) G. H. Hea, G. L. Hea, A. J. Lia, X. Lia, X. J. Wang, Y. P. Fang, Y. H. Xua, *J. Mol. Catal. A: Chem.*, 2014, **385**, 106.

CrystEngComm Accepted Manuscript

131 K. C. Leonard, K. M. Nam, H. Chan Lee, S. H. Kang, H. S. Park and A. J. Bard, *J. Phys. Chem. C.*, 2013, **117**, 15901..

132 J. E. Yourey, J. B. Kurtz and B. M. Bartlett, *J. Phys. Chem. C.,* 2012, **116**, 3200.

133 M. M. Mohamed, S. A. Ahmed and K. S. Khairou, *Appl. Catal. B: Environ.*, 2014, **150– 151**, 63.

134 (a) S. J. Hong, S. Lee, J. S. Jang and J. S. Lee, *Energy Environ. Sci.*, 2011, **4**, 1781; (b) M. Ma, J. K. Kim, K. Zhang, X. Shi, S. J. Kim, J. H. Moon and J. H. Park, *Chem. Mater.*, 2014, **26**, 5592.

135 S. K. Pilli, R. Janarthanan, T. G. Deutsch, T. E. Furtak, L. D. Brown, J. A. Turner and A. M. Herring, *Phys. Chem. Chem. Phys.*, 2013, **15**, 14723.

136 T. Jin, P. Diao, Q. Wu, D. Xu, D. Hu, Y. Xie and M. Zhang, *Appl. Catal. B: Environ.*, 2014, **148–149**, 304.

137 R. Saito, Y. Miseki and K. Sayama, *Chem. Commun.*, 2012, **48**, 3833.

138 W. Kim, T. Tachikawa, D. M. Satoca, H. i. Kim, T. Majima and W. Choi, *Energy Environ. Sci.*, 2013, **6**, 3732.

139 H. Huang, Z. Yue, G. Li, X. Wang, J. Huang, Y. Du and P. Yang. *J. Mater. Chem. A*, 2013, **1**, 15110.

140 A. A. Taha and F. Li, *Catal. Sci. Technol.*, 2014, **4**, 3601.

141 C. Janaky, N. R. D. Tacconi, W. Chanmanee and K. Rajeshwar, *J. Phys. Chem. C.*, 2012, **116**, 4234.

142 S. Anandan and M. Miyauchi, *Chem. Commun.*, 2012, **48**, 4323.

143 H. Katsumata, Y. Oda, S. Kaneco and T. Suzuki, *RSC Adv.*, 2013, **3**, 5028.

144 R. Solarska, K. Bienkowski, S. Zoladek, A. Majcher, T. Stefaniuk, P. J. Kulesza and J. Augustynski, *Angew. Chem. Int. Ed*. 2014, **53**, 14196.

145 R. Solarska, A. Krolikowska and J. Augustynski. *Angew. Chem. Int. Ed.*, 2010, **49**, 7980.

146 (a) R. Abe, H. Takami, N. Murakami and B. Ohtani, *J. Am. Chem. Soc.*, 2008, **130**, 7780; (b) K. Wenderich, A. Klaassen, I. Siretanu, F. Mugele and G. Mul, *Angew. Chem. Int. Ed.*, 2014, **53**, 12476.

147 A. Tanaka, K. Hashimoto and H. Kominami, *J. Am. Chem. Soc.*, 2014, **136**, 586.

148 R. N. Dominey , N. S. Lewis , J. A. Bruce , D. C. Bookbinder and M. S. Wrighton, *J. Am. Chem. Soc.*, 1982, **104**, 467.

149 Y. J. Hwang, A. Boukai and P. Yang, *Nano Lett.*, 2009, **9**, 410.

150 J. Shi, Y.Hara, C. Sun, M. A. Anderson and X. Wang, *Nano Lett.*, 2011, **11**, 3413.

151 S. K. Pilli, T. G. Deutsch, T. E. Furtak, L. D. Brown, J. A. Turner and A. M. Herring, *Phys. Chem. Chem. Phys.*, 2013, **15**, 3273.

152 A. Paracchino, V. Laporte, K. Sivula1, M. Gratzel1and E. Thimsen, *Nat. Mater.*, 2011, **10**, 456.

153 J. Huang and Q. Wan, *Sensors*, 2009, **9**, 9903.

154 A. Rydosz, W. Maziarz, T. Pisarkiewicz, K. Wincza and S. Gruszczyński, SDIWC digital library, 2014, 150-155.

155 M. J. Natan, T. E. Mallouk and M. S. Wrighton, *J. Phys. Chem.*, 1987, **91**, 648.

156 L. Santos, J. P. Neto, A. Crespo, D. Nunes, N. Costa, I. M. Fonseca, P. Barquinha, L. Pereira, J. Silva, R. Martins and E. Fortunato, *ACS Appl. Mater. Interfaces*, 2014, **6**, 12226.

157 (a) I. Jimenez, M.A. Centeno, R. Scotti, F. Morazzoni, J. Arbiol, A. Cornet and J. R. Morante, *J. Mater. Chem.,* 2004, **14**, 2412; (b) A. Ponzoni, E. Comini, G. Sberveglieri, J. Zhou, S. Z. Deng, N. S. Xu, Y. Ding and Z. L. Wang, *Appl. Phys. Lett.*, 2006, **88**, 203101; (c) O. M. Conanec, P.T. Moseley, *J. Mater. Chem.,* 2002, **12**, 1779; (d) B. Cao, J. Chen, X. Tang, W. Zhou, *J. Mater. Chem.,* 2009, **19**, 2323; (e) C. S. Rout, A. Govindaraj and C. N. R. Rao, *J. Mater. Chem.,* 2006, **16**, 3936.

158 (a) H. Nakagawa, N. Yamamoto, S. Okazaki, T. Chinzei and S. Asakura, *Sens. Actuators B,* 2003, **93**, 468; (b) L. F. Zhu, J. C. She, J.Y. Luo, S. Z. Deng, J. Chen and N. S. Xu, *J. Phys. Chem. C,* 2010, **114**, 15504; (c) H. J. Chen, N. S. Xu, S. Z. Deng, D. Y. Lu, Z. L. Li, J. Zhou and J. Chen, *Nanotechnology,* 2007, **18**, 205701.

159 S. Park, H. Kim, C. Jin, S. W. Choi, S. S. Kim and C. Lee, *Thermochimica Acta*, 2012, **542**, 69.

160 Y. Qin, F. Wang, W. Shen and M. Hu, *J. Alloys Compd.,* 2012, **540**, 21.

161 S. J. Choi, C. Choi, S. J. Kim, H. J. Cho, S. Jeon and I. D. Kim, *RSC Adv.*, 2015, **5**, 7584.

162 M. Righettoni, A. Tricoli and S. E. Pratsinis, *Anal. Chem.,* 2010, **82**, 3581.

163 J. Xiao, P. Liu, Y. Liang, H. B. Li and G. W. Yang, *Nanoscale*, 2012, **4**, 7078.

164 C. L. Dai, M. C. Liu, F. S. Chen, C. C. Wu and M. W. Chang, *Sens. Actuators B*, 2007, **123**, 896.

165 M. Bendahan, J. Gu´erin, R. Boulmani and K. Aguir, *Sens. Actuators B,* 2007, **124**, 24.

166 N. Parvatikar, S. Jain, S. Khasim, M. Revansiddappa, S.V. Bhoraskar and M. V. N. Ambika Prasad, *Sens. Actuators B*, 2006, **114,** 599.

167 H. Li, B. Liu, D. Cai, Y. Wang, Y. Liu, L. Mei, L. Wang, D. Wang, Q. Li and T. Wang, *J. Mater. Chem. A*, 2014, **2**, 6854.

168 Y. Peng, J. Li, L. Chen, J. Chen, J. Han, H. Zhang and W. Han, *Environ. Sci. Technol.*, 2012, **46**, 2864.

169 C. Shifu, J. Lei, T. Wenming and F. Xianliang, *Dalton Trans.*, 2013, **42**, 10759.

170 B. Lu, X. Li, T. Wang, E. Xie abd Z. Xu, *J. Mater. Chem. A,* 2013, **1**, 3900

171 Y. Liu, Q. Li, S. Gao and J. K. Shang, *Cryst. Eng. Comm.*, 2014, **16**, 7493.

172 H. Qi, J. Wolfe, D. Wang, H. J. Fan, D. Fichou and Z. Chen, *Nanoscale*, 2014, **6**, 13457.

173 J. Liu, S. Han, J. Li and J. Lin, *RSC Adv.*, 2014, **4**, 37556.

174 S. H. Lee, R. Deshpande, P. A. Parilla, K. M. Jones, B. To, A. H. Mahan and A. C. Dillon, *Adv. Mater.,* 2006, **18**, 763.

175 I. Kostis, M. Vasilopoulou, A. Soultati, P. Argitis, N. Konofaos, A.M. Douvas, N. Vourdas, G. Papadimitropoulos and D. Davazoglou, *Microelectron. Eng.,* 2013, **111**, 149.

176 Y. C. Her and C. C. Chang, *CrystEngComm.*, 2014, **16**, 5379.

177 D. Ma, G. Shi, H. Wang, Q. Zhang and Y. Li, *J. Mater. Chem. A*, 2013, **1**, 684.

178 G. F. Cai, D. Zhou, Q. Q. Xiong, J. H. Zhang, X. L. Wang, C. D. Gu and J. P. Tu, *Sol. Energy Mater. Sol. Cells*, 2013, **117**, 231.

179 B. Gavanier, F.M. Miehalak and J. R. Owen, *Ionics*, 1997, **3**, 265.

180 I. Turyan, U. O. Krasovec, B. Orel, T. Saraidorov, R. Reisfeld and D. Mandler, *Adv. Mater.,* 2000, **12**, 330.

181 M. R. Kumar, G. M. A. Rahman, D. J. Thomson and M. S. Freund, *Chem. Commun.,* 2012, **48**, 9409.

182 C. H. Chen, T. C. Chang, I. H. Liao, P. B. Xi, J. Hsieh, J. Chen, T. Huang, S. M. Sze, U. S. Chen and J. R. Chen, *Appl. Phys. Lett.*, 2008, **92**, 013114.

183 Patnaik, Pradyot. Handbook of Inorganic Chemical Compounds. McGraw-Hill, 2003.

184 F. Wang, Y. Li, Z. Cheng, K. Xu, X. Zhan, Z. Wang and J. He, *Phys. Chem. Chem. Phys.,* 2014, **16**, 12214.

185 *H. Hayashia and A. Ishizaka, Appl. Phys. Lett.,* 2003, **82**, 1365

186 *J. Y. Kim, J. H. Kang, D. Y. Jeon and Y. C. You, Technical Digest of lVMC, 2003.*